Communications Biology

https://doi.org/10.1038/s42003-026-09825-2

Article in Press

Normative modeling of MEG brain oscillations across the human lifespan

Received: 14 July 2025

Accepted: 25 February 2026

Cite this article as: Zamanzadeh, M., Verduyn, Y., Boer, A. *et al.* Normative modeling of MEG brain oscillations across the human lifespan. *Commun Biol* (2026). https://doi.org/10.1038/s42003-026-09825-2

Mohammad Zamanzadeh, Ymke Verduyn, Augustijn de Boer, Tomas Ros, Thomas Wolfers, Richard Dinga, Marie Šafář Postma, Andre F. Marquand, Marijn van Wingerden & Seyed Mostafa Kia

Normative Modeling of MEG Brain Oscillations Across the Human Lifespan

Mohammad Zamanzadeh[1*] Ymke Verduyn[1] Augustijn de Boer[2,3]
Tomas Ros[4] Thomas Wolfers[5,6] Richard Dinga[1] Marie Šafář Postma[1]
Andre F. Marquand[2,3] Marijn van Wingerden[1] Seyed Mostafa Kia[1,2,7*]

[1] Center of Cognitive Science and Artificial Intelligence, Tilburg University, Tilburg, the Netherlands
[2] Donders Institute for Cognition, Brain and Behavior, Radboud University, Nijmegen, The Netherlands
[3] Department of Cognitive Neuroscience, Radboud University Medical Center, Nijmegen, The Netherlands
[4] CIBM Center for Biomedical Imaging, University of Geneva, Geneva, Switzerland
[5] Department of Psychiatry and Psychotherapy, University Hospital Tübingen, Tübingen, Germany
[6] German Center for Mental Health, University of Tübingen, Tübingen, Germany
[7] Department of Psychiatry, UMC Utrecht Brain Center, University Medical Center, Utrecht, the Netherlands
[*] Corresponding authors, e-mails: m.zamanzadehnasrabadi@tilburguniversity.edu, s.m.kia@tilburguniversity.edu

February 25, 2026

Abstract

Normative modeling provides a principled framework for quantifying individual deviations from typical brain development and is increasingly used to study heterogeneity in neuropsychiatric conditions. While widely applied to structural phenotypes, functional normative models remain underdeveloped. Here, we introduce MEGaNorm, a normative modeling framework for charting lifespan trajectories of resting-state magnetoencephalography (MEG) brain oscillations. Using a large, multi-site dataset comprising 1,846 individuals aged 6–88 and spanning three MEG systems, we model relative oscillatory power in canonical frequency bands using hierarchical Bayesian regression, accounting for age, sex, and site effects. To support interpretation at multiple scales, we introduce Neuro-Oscillo Charts, visual tools that summarize normative trajectories at the population level and quantify individual-level deviations, enabling personalized assessment of functional brain dynamics. Applying this framework to a Parkinson's disease cohort (n = 160), we demonstrate that normative deviation scores reveal disease-related abnormalities and identify a continuum of patients in the theta–beta deviation space. This work establishes a multi-site normative reference for resting-state MEG oscillations (3–40 Hz) across a broad age range, enabling population-level characterization and individualized benchmarking. All models and tools are openly available and designed for federated, continual adaptation as new data become available, providing a methodological foundation toward precision neuropsychiatry.

Introduction

Normative modeling[1,2] has emerged as a transformative approach in neuroimaging, providing a robust framework to characterize individual deviations from typical brain structure and function by establishing population-level reference distributions. Traditional case–control studies assume distinct case and control groups and rely on group-averaged comparisons, with the group means treated as representative of individuals within that cohort. This assumption imposes a pairwise mapping between diagnostic categories and neurophysiological underpinnings, which can obscure biologically meaningful variability across individuals[3]. In contrast, normative models explicitly account for this individual-level variability by enabling subject-specific quantification of deviations from population norms[1,2]. This approach captures the continuous nature of brain variation across demographic and clinical populations[4]. It has been particularly impactful in structural magnetic resonance imaging (sMRI) studies, where it is used to map deviations in patients with neuropsychiatric disorders using various imaging phenotypes, such as cortical thickness[5], subcortical volumes[6], and white matter microstructure[7,8]. For example, in schizophrenia[9,10] and autism spectrum disorder[11], normative models have uncovered distinct neuroanatomical alterations and identified subgroups of patients with atypical developmental trajectories that remain undetected using conventional group-based analyses[3]. Similarly, in Alzheimer's disease, normative approaches have helped disentangle age-related atrophy from disease-specific pathological changes[12,13]. By providing individualized deviation profiles, normative modeling represents a crucial step toward precision medicine[14,15], offering a data-driven framework for understanding disease heterogeneity and informing personalized diagnostic and therapeutic strategies.

While normative models of sMRI have shown considerable promise in advancing precision neuropsychiatry, extending this framework to functional neuroimaging modalities is essential for deepening our understanding of complex brain disorders and diseases. Many neuropsychiatric conditions are defined by abnormal functional brain dynamics, which can be studied using techniques such as functional MRI (fMRI), electroencephalography (EEG), and magnetoencephalography (MEG)[16–18]. Normative modeling has already been applied to fMRI data to establish normative maps of functional brain dynamics[19–21]. However, normative models for EEG and MEG data are still underdeveloped, despite their high temporal resolution and ability to capture neuronal dynamics[22–24], reflecting key functional processes including sensory integration, attention, and memory[25,26].

Understanding how brain oscillations evolve across the lifespan has long been a central objective in neuroscience. Early efforts in this area focused on EEG and introduced foundational approaches to characterize normative brain activity[27–29]. While these studies pioneered the concept of normative baselines for electrophysiological signals, they relied on relatively simple parametric models and were often constrained by small or demographically narrow samples. More recently, advances in data acquisition and processing have enabled more detailed lifespan analyses using both EEG[30–33] and MEG[34–41]. For example, Rempe et al.[40] quantified age-related changes in relative and absolute power across the lifespan in resting-state MEG (rs-MEG). Elsewhere, Thuwal et al.[38] and Hinault et al.[42] examined age-related changes in both oscillatory and non-oscillatory measures and their associations with different cognitive

functions. Tröndle et al.[43] examined alpha-band power development in adolescents using data from the Human Brain Network. While these studies have offered valuable insights into mean trends across age, they did not model the full distribution of individual variability using centile-based approaches. As a result, inter-individual heterogeneity, essential for applications in precision medicine, is not fully captured. Furthermore, the reliance on single-site datasets with restricted age ranges limits their generalizability across devices and the full human lifespan.

In this study, we introduce the MEGaNorm framework, an end-to-end rs-MEG processing pipeline for 1) deriving lifespan normative ranges of functional imaging-derived phenotypes (IDPs) on large, multi-scanner MEG datasets, and 2) mapping individuals' IDPs to their deviations from the norm of the population. Using this framework, we derive normative models of rs-MEG oscillations for the relative power spectrum density of theta, alpha, beta, and gamma frequency bands after removing the aperiodic component of the signal. By isolating periodic activity, our normative models capture age-related spectral power changes of neural oscillations, independent of broadband power shifts in absolute power[44]. The models are constructed using large-scale rs-MEG data from multiple scanners and hardware vendors. To account for this inter-site variability, we employ hierarchical Bayesian regression (HBR)[5,45], which enables simultaneous estimation of non-Gaussian and heteroscedastic age-specific centiles of variation in brain oscillations while modeling site-specific effects.

We further show how the derived normative models can be used to systematically characterize changes in lifespan trajectories of resting-state brain oscillations at the population level, as well as individual deviations from the population norm. At the population level, we estimate growth charts of relative spectral powers with different trajectories for male and female populations across the lifespan. Using these growth charts, we derive Population-level Neuro-Oscillo Charts (P-NOCs), which show how the relative distribution of brain oscillations in theta, alpha, beta, and gamma frequency bands changes across the human lifespan. At the individual level, we introduce Individual-level Neuro-Oscillo Charts (I-NOCs), which map individual spectral power measurements onto population norms, conditioned on age, sex (following the SAGER guidelines[46], we use the term "sex" limited to "female" and "male"), and scanning device. I-NOCs enable a fine-grained assessment of individual deviations, offering a personalized interpretation of brain dynamics concerning the normative range of brain oscillations in a reference population. Finally, to demonstrate the translational utility of our framework, we benchmark our model on a cohort of patients with Parkinson's disease, leveraging normative deviation scores to quantify oscillatory abnormalities within the patient population. We show how normative models can help conceptualize a neuropsychiatric disorder as a continuum of abnormalities in IDPs, highlighting their potential for precision neuropsychiatry.

Results

We developed MEGaNorm, a normative modeling framework to chart lifespan trajectories of MEG brain oscillations and to identify individual deviations from these normative ranges. We used rs-MEG recordings from 1,846 healthy individuals aged 6–88 and a clinical cohort of 160 individuals with Parkinson's

disease aged 43–88. These data were pooled from six independent datasets acquired using three major MEG systems (see Datasets), offering broad coverage of the human lifespan and diverse acquisition environments. This dataset was used to derive reference models of IDPs, defined as sensor-level relative power in canonical frequency bands.

To derive these normative models, MEGaNorm integrates a sequence of processing and modeling steps illustrated in Figure 1. Figure 1a outlines the preprocessing and feature extraction pipeline: resting-state MEG recordings undergo band-pass filtering, artifact removal, and segmentation into fixed-length epochs. Power spectral densities (PSDs) are then computed and decomposed into periodic and aperiodic components to isolate oscillatory activity. Relative power in the theta, alpha, beta, and gamma bands is extracted from the periodic component and averaged across sensors to yield device-agnostic oscillatory neural measurements. We refer to these measurements as imaging-derived phenotypes (IDPs), aligning with the broader use of the term to denote quantitative summaries derived from functional and structural neuroimaging modalities[47,48].

In the next stage (Figure 1b), we use these IDPs to construct normative reference models from a large, multi-site cohort of healthy participants. Lifespan trajectories for each frequency band are estimated using hierarchical Bayesian regression (HBR)[5,49,45], which accounts for non-Gaussian distributions, heteroscedasticity, and site- and sex-specific effects. The resulting models yield age- and sex-conditioned centiles that serve as a robust normative reference for subsequent applications.

We then apply these models for individual deviation analysis (Figure 1c), where new subject data are processed using the same pipeline to extract IDPs. These are mapped onto the normative models to compute centile-based deviation scores. This two-stage framework, normative model estimation followed by individual deviation analysis, enables diagnosis-agnostic application and supports a range of clinical use cases, including early diagnosis, individualized treatment monitoring, and stratification based on functional brain profiles. Full methodological details are provided in Methods.

Model evaluation: modeling non-gaussianity, heteroscedasticity, and non-linearity results in more accurate centiles

We evaluated the quality of the fitted normative models using both quantitative and qualitative out-of-sample diagnostics. We performed an ablation study comparing our proposed non-linear, heteroscedastic, and non-Gaussian HBR model (see section for details) to a simplified baseline. The proposed model used a B-spline basis for age, a Sinh-Arcsinh (SHASH) likelihood[50,45], and modeled variance as a function of age. In contrast, the baseline model employed a linear age term, a Gaussian likelihood, and assumed homoscedastic variance. This comparison aimed to determine whether incorporating flexible distributional assumptions improves the fidelity of normative centile estimates.

Both models were evaluated using repeated 50%–50% train–test splits of healthy participants, stratified by site (see Section for details). Model training and evaluation were repeated 10 times using different random seeds for train–test splits to assess the stability and generalizability of performance. A range of evaluation metrics was used to assess both the location and shape of the fitted distributions. To

quantify the accuracy of the fitted curve at the median (50^{th} percentile), we computed the standardized mean squared error (SMSE), which evaluates how well the model predicts the central tendency of the data. To evaluate the distributional properties of the derived z-scores as a measure of model calibration, we calculated skewness, excess kurtosis, and the Shapiro–Wilk test statistic (W)[51]. To directly assess the accuracy of centile estimation, we used the mean absolute centile error (MACE), introduced in this study for evaluating the calibration of estimated centiles (see Section for more information). Results are summarized in Figure 2. As a complementary qualitative assessment, Q–Q plots were used to visually evaluate the alignment between empirical and theoretical Gaussian quantiles.

Although both models performed similarly in predicting the central tendency, quantified by SMSE, with significant improvement observed only in the theta band (see Table 1), the proposed HBR model provided substantially better estimates of the full distributional shape. Across all frequency bands, z-score distributions derived from the proposed model more closely approximated a standard Gaussian distribution, as reflected in W statistics closer to 1.0 and skewness and excess kurtosis values nearer to zero. While mild leptokurtosis remained, the distributions exhibited improved symmetry and tail behavior. These improvements were visually corroborated by Q–Q plots (Figure 2b), which showed tighter alignment between empirical and theoretical quantiles. Additionally, the proposed model achieved significantly lower MACE values across all frequency bands (Wilcoxon rank-sum test $p < 0.05$), indicating superior centile calibration. Together, these findings suggest the proposed model more accurately captures the shape of the underlying distributions, an essential feature for deriving well-calibrated normative centiles. This supports the inclusion of non-Gaussianity, heteroscedasticity, and non-linearity in modeling the IDPs.

Population- and individual-level Neuro-Oscillo Charts

Building on the accuracy of the proposed HBR model, we used the full dataset of healthy individuals to derive growth charts for four oscillatory IDPs. These charts were generated by sampling from the posterior predictive distribution across ages 6 to 80, separately for males and females (Figure 3a). The resulting centile trajectories reveal substantial inter-individual variability and exhibit complex age-related dynamics, including heteroscedasticity and non-linear trends.

To summarize normative developmental patterns at the population level, we introduce Population-level Neuro-Oscillo Charts (P-NOCs), which visualize age-related changes in the relative power of frequency bands for 5-year intervals (ages 5 to 80) at the median (50^{th}) centile. P-NOCs illustrate the relative contribution of each frequency band's 50^{th} centile to the total power spectra. Figure 3b shows P-NOCs for male and female populations. These charts reveal key lifespan trends: theta power follows a U-shaped trajectory with a minimum in midlife (ages 30–40), alpha power follows an inverted U-shaped trend peaking in early adulthood (ages 20–30), beta power increases steadily until age 50, and slow gamma remains relatively constant, albeit small in magnitude. Notably, we observe a shift in compensatory dynamics around age 50: before this point, declining alpha power is offset by increasing beta power, whereas after age 50, beta power plateaus and the decline in alpha is accompanied instead by increasing theta power.

To enable individualized interpretation and enhance the clinical utility of the model, we further introduce Individual-level Neuro-Oscillo Charts (I-NOCs), which allow single-subject benchmarking against normative trajectories. I-NOCs visualize an individual's IDP values in relation to the reference normative range, conditioned on the participant's demographic information. Figure 3c illustrates I-NOCs for a healthy participant, conditioned on the participant's age, sex, and recording site (a 54-year-old female participant from the Cam-CAN dataset), whose values fall within the normal range across all frequency bands. For example, theta's I-NOC shows that theta power accounts for 13.4% of the total oscillatory power, which is 3.9% below the population median (50th percentile), yet remains within the normal range (i.e., between 25^{th} to 75^{th} percentiles). I-NOCs offer an intuitive and scalable tool for personalized IDP profiling, providing a foundation for real-time downstream applications in anomaly detection and patient stratification.

Deviations from normative ranges are informative in Parkinson's disease

We evaluated the clinical utility of the derived normative models in an anomaly detection framework by assessing whether large deviations from normative ranges could identify individuals with Parkinson's disease. This was done using models trained exclusively on data from healthy individuals, without any exposure to patients' data[5]. Specifically, we used the OMEGA dataset, selecting 221 undiagnosed participants from the test partition as controls and 160 Parkinson's disease patients from the same dataset as the clinical cohort. Although the two groups were not age-matched, this does not confound the analysis because all the downstream analyses are performed in the z-score space, where the age effects are regressed out in the normative modeling process by including age as a covariate.

For each participant, deviation scores (z-scores) were computed and converted into abnormal probability indices using the method introduced in Kia et al. [5] (see also Methods for details). We then evaluated the discriminative power of each frequency-specific IDP by calculating the area under the receiver operating characteristic curve (AUC). Statistical significance ($p < 0.05$) was assessed using permutation testing (1000 repetitions), with false discovery rate (FDR) correction for multiple comparisons[52]. This procedure was repeated across 10 different random train-test splits of the healthy cohort, while the same Parkinson's disease cohort was used in each iteration.

Figure 4a summarizes AUC results across ten runs. Among the four IDPs, theta z-scores showed the strongest discriminative performance (mean AUC = 0.62, SD = 0.01), significantly outperforming chance in all iterations. Beta z-scores also demonstrated significant predictive power (mean AUC = 0.59, SD = 0.01) across all runs. In contrast, gamma z-scores (mean AUC = 0.53, SD = 0.02) were significant in only 2 out of the 10 runs, and alpha z-scores (mean AUC = 0.45, SD = 0.008) failed to reach significance in any run. These findings suggest that deviations in theta and beta band power are informative markers of disease-related functional abnormalities.

Decoding heterogeneity in patients via theta-beta deviation profiles

To further characterize the directionality and heterogeneity of observed abnormalities in Parkinson's patients, we examined the distribution of extreme deviations ($|Z| > 2$) in IDPs among patients. As shown in Figure 4b, 13.43% of patients exhibited positive extreme deviations ($Z > 2$) in the theta band, while 9.06% showed negative extreme deviations ($Z < -2$) in the beta band. Additionally, 8.12% of patients displayed negative deviations in gamma power. Deviations in the alpha band, by contrast, were infrequent and not substantial.

To characterize patterns of variability in patients, we visualized the joint distribution of patients in theta–beta deviation space, corresponding to the two frequency bands that showed the strongest deviations in the anomaly detection analysis (see Supplementary Figure 1 for theta–gamma and beta–gamma deviation spaces). As shown in Figure 4c, this representation reveals a continuum of oscillatory deviation profiles, ranging from high-theta/low-beta to low-theta/high-beta. Notably, a subset of individuals falls within the interquartile range of the normative distribution for both bands, indicating relatively preserved oscillatory profiles. Overall, this continuum reflects variability in patients' deviation profiles that may arise from multiple, potentially interacting factors, including disease heterogeneity, differences in disease stage, and medication-related effects.

To illustrate this variability more concretely, we present I-NOCs for four representative patients with Parkinson's disease (P1–P4) located at different points along the theta–beta deviation spectrum. These I-NOCs reveal that patients diagnosed with the same condition can exhibit markedly different neurophysiological profiles, falling in different quantile ranges of the norm. Patients P1 and P4 are positioned toward opposite extremes of the spectrum: P1 shows extremely low relative theta power (5.0%) and extremely high beta power (80.1%), whereas P4 exhibits the opposite pattern, with extremely high theta (83.8%) and extremely low beta (2.6%). In contrast, patients P2 and P3 display large deviations in only one of the frequency bands. P3's beta power (8.7%) is extremely low, while its theta deviation falls within the normal range. Conversely, P2 has relatively normal beta power (20.1%, within the interquartile range), but extremely elevated theta. These examples highlight the utility of normative modeling in capturing individual variability across patients.

Discussion

In this study, we addressed the long-standing challenge of delineating normative developmental trajectories of brain oscillations across the human lifespan[27,28,30,34,35,40,42,53,33,39,54–56]. To this end, we introduced MEGaNorm, a normative modeling framework for estimating age-related centiles of IDPs based on large-scale, multi-site rs-MEG data covering ages 6 to 88. The derived models offer a transdiagnostic solution by providing normative reference distributions not constrained by diagnostic categories, thereby supporting applications across a wide range of neuropsychiatric conditions. To demonstrate clinical relevance, we applied MEGaNorm to a Parkinson's disease cohort and showed that deviation scores captured individual-specific functional abnormalities that would be obscured in conventional case-control analyses.

These results are consistent with the dimensional approach that emphasizes characterizing mental disorders along continuous axes of neurobiological variation. In the following, we outline key methodological advances introduced by MEGaNorm that extend the current state of the art and offer substantial value for both basic and translational neuroscience.

To enhance the specificity of the derived oscillatory IDPs, we isolated periodic brain oscillations from the aperiodic component of the MEG signal. Electrophysiological recordings inherently contain both oscillatory (periodic) activity and a broadband aperiodic background, which includes neural and non-neural contributions such as instrumental noise and physiological artifacts[43,57,44]. Aperiodic features have been shown to vary systematically with age[58–60], arousal[61], individual factors like educational background[62], cognitive functions[63,38,42], and cardiac artifacts[60]. Failing to account for these influences can obscure true oscillatory dynamics[64,65,63]. By separating these components before feature extraction, MEGaNorm yields a more accurate and interpretable quantification of spectral power, thereby supporting a more reliable characterization of normative brain oscillations across the lifespan. Although the present study focused on periodic features, the framework is equally suited for modeling normative trajectories of aperiodic components whose relevance to cognitive aging and neuropsychiatric conditions is increasingly recognized[38,63,66].

To ensure generalizability and robust estimation of normative trajectories, we constructed our models using a large, multi-site dataset comprising recordings from multiple MEG hardware systems. This design choice allowed us to better capture population-level variability and improve the applicability of the derived centiles across diverse acquisition settings. The estimation of reliable centiles in normative modeling, particularly when using flexible methods such as HBR, critically depends on large sample sizes[6,67]. To address this need, we aggregated six independent rs-MEG datasets spanning a wide age range and three different MEG manufacturers. While this multi-site strategy introduces valuable diversity, it also presents challenges due to scanner and protocol-specific differences, environmental noise, and sample heterogeneity[68]. We mitigated these effects by modeling the site as a batch variable in HBR using partial pooling[5], enabling the model to share information across sites while retaining sensitivity to systematic inter-site differences (see Supplementary Results 1). This principled handling of site effects enhances the robustness and transferability of the resulting normative models.

We adopted a flexible normative modeling framework based on HBR to accommodate non-Gaussian distributions, heteroscedasticity, and nonlinear age-related trends. This methodological flexibility was critical for producing accurate, data-driven growth charts that capture both the central tendency and dispersion of IDPs across the lifespan. Earlier studies have reported inter-individual variability in the healthy aging of brain oscillations using descriptive tools such as box plots[34], confidence intervals[69], or by noting wide deviations around mean trajectories[70,36]. Such variability is likely shaped by diverse biological and environmental influences, including genetic factors, neurodevelopmental differences, and contextual exposures [71–73]. Capturing this variability requires models that not only estimate the mean developmental trajectory but also account for the distributional shape and its evolution with age. Empirical findings have demonstrated that the variance and skewness of oscillatory power can vary substantially with age[34,74], and that transformations are often needed to approximate Gaussianity in EEG datasets[75].

Moreover, studies have shown that nonlinear trends, such as quadratic patterns, are better suited for modeling changes in different frequency bands across the lifespan [36,37,40]. To address these challenges, we employed a semi-parametric modeling strategy using B-spline basis functions, which enables flexible estimation of nonlinear trajectories without imposing rigid parametric assumptions [76]. Our findings confirmed that the resulting growth charts accurately reflect non-Gaussian, heteroscedastic variation in IDPs.

The MEGaNorm framework is inherently extensible and designed to accommodate calibration on new, local, or private datasets [5]. As additional data become available, posterior distributions from pre-trained models can be leveraged as informative priors, enabling model refinement without requiring re-estimation from scratch. This feature is particularly valuable for sites with limited sample sizes or restricted age ranges, as it enables partial pooling across datasets while preserving sensitivity to site-specific effects. Notably, prior work has shown that even small calibration cohorts, as few as 25 participants, are sufficient to adapt HBR-based models to new populations [77]. Crucially, this adaptation does not necessitate centralized data sharing: the hierarchical structure of HBR supports federated learning, allowing models to be updated locally while maintaining data privacy and regulatory compliance. To facilitate broader adoption, the data processing pipeline and derived models are openly shared, respectively via the MEGaNorm package [78] and PCNPortal [79], supporting reproducibility and enabling continual improvement as the community contributes new data.

We also introduced two complementary visualization tools, P-NOCs and I-NOCs, that enhance the interpretability of normative modeling outputs at both the population and individual levels. P-NOCs depict how the relative contributions of canonical frequency bands proportionally evolve with age. These charts serve as compact summaries of developmental and aging trajectories, facilitating population-level comparisons across demographic groups. In contrast, I-NOCs provide subject-specific benchmarking by situating an individual's spectral power profile within the normative distribution, conditioned on individuals' demographic information such as age, sex, and recording site. I-NOCs enable personalized assessments that are especially useful in clinical applications, including early diagnosis and monitoring of treatment effects.

To demonstrate the clinical utility of MEGaNorm, we applied the framework to a cohort of individuals with Parkinson's disease, a condition known to involve widespread disruptions in neural oscillatory dynamics [80–83]. A well-documented feature of Parkinson's disease is neural slowing, typically characterized by elevated power in lower-frequency bands (e.g., theta and alpha) and reduced power in higher-frequency bands (e.g., beta and gamma) [84,85]. However, these patterns are inconsistently observed across studies, with variability attributed to differences in patient subgroups [84], disease stages [86,87], and methodological factors. In particular, some studies report no significant differences in alpha or beta power between patients and controls [88,89], and the effects of dopamine replacement therapy on oscillatory power remain equivocal [87,90]. These discrepancies likely reflect the clinical and biological heterogeneity of Parkinson's disease [91,92], as well as the limitations of conventional case-control analyses that rely on group-averaged contrasts, which can obscure meaningful inter-individual variation [3,93]. Normative modeling offers a principled alternative by estimating individual-level deviations from a population-based reference, thus

enabling the characterization of functional abnormalities along a continuous spectrum rather than dichotomous case-control categories[4,1].

Using the normative modeling approach within an anomaly detection framework[5], we identified significant deviations in theta and beta frequency bands among individuals with Parkinson's disease, with average AUCs of 0.62 and 0.59, respectively. These findings highlight theta and beta power as informative markers of disease-related functional alteration. Notably, these results were obtained using models trained exclusively on healthy participants in an unsupervised manner, without incorporating diagnostic labels. Unlike traditional classification approaches that aim to distinguish between diagnostic groups, normative modeling quantifies how each individual deviates from population norms conditioned on age, sex, and recording site. Despite not being tailored to Parkinson's disease, the models successfully captured clinically meaningful deviations, supporting their utility for probing functional heterogeneity. This unsupervised and diagnosis-agnostic nature of the framework underscores its generalizability and applicability across diverse neuropsychiatric conditions.

To further investigate the structure of abnormalities in theta-beta deviation space, we analyzed the joint distribution of theta and beta z-scores. While a subset of individuals displayed marked increases in theta and reductions in beta power, consistent with the neural slowing profile commonly reported in Parkinson's disease[84,85], other patients showed minimal or no deviation from normative centiles. This inter-individual variability was captured in a two-dimensional z-score space, which revealed a continuum of profiles ranging from high-theta/low-beta to low-theta/high-beta. These patterns highlight the substantial heterogeneity in both the direction and magnitude of deviations[84,86,87], reinforcing the perspective that neuropsychiatric diseases are best conceptualized as a spectrum of functional brain alterations rather than a uniform neurophysiological entity[4,1,2].

While this study provides a foundational framework for functional normative modeling using MEG, several methodological limitations merit consideration. From a dataset composition perspective, although our sample is large and drawn from multiple sites, it remains underrepresented in terms of ethnically and socioeconomically diverse populations, with the majority of participants recruited from Western countries. This limits the global generalizability of the normative reference. In addition, the clinical demonstration using Parkinson's disease data relies on a single publicly available cohort, and therefore does not yet assess the robustness of deviation patterns across independent acquisition protocols and populations. An important direction for future work is the replication and extension of these analyses across additional clinical datasets. Crucially, the federated architecture of HBR supports decentralized model updates without requiring data sharing[5]. This design enables the normative reference and associated clinical evaluations to be progressively expanded and validated on additional data from demographically and culturally diverse samples, expanding its inclusivity and clinical generalizability.

In terms of preprocessing, spectral analyses were restricted to the 3–40 Hz range due to limitations of the specparam method[57], precluding investigation of the delta frequency band. Given the importance of this frequency band[24,94,95], alternative methods for separating periodic and aperiodic activity, such as irregular-resampling auto-spectral analysis (IRASA)[96], may help extend modeling across the full frequency spectrum. Additionally, oscillatory features were computed and averaged at the sensor level to

ensure comparability across different MEG systems. Even though this aggregation reduces spatial specificity, it facilitates device-agnostic harmonization, ensuring comparability across different MEG systems with varying sensor counts and locations, and enhances transferability to lower-resolution platforms such as EEG or portable devices. Source-space modeling offers the potential to improve anatomical localization of functional features, particularly in datasets with co-registered structural MRI. Future extensions of MEGaNorm will incorporate source-reconstructed data to enhance spatial specificity. To ensure accuracy, such extensions should also account for age-related changes in head conductivity and skull thickness, which are known to affect source estimates and may introduce systematic biases if not properly modeled[97,98].

To further enhance the clinical applicability of our approach, several key extensions should be explored. First, our analysis of the Parkinson's disease cohort did not account for medication status or disease staging, as such metadata were not publicly available. Prior research has shown that both factors can substantially influence neural oscillatory patterns[85,99,100], and incorporating them in future work may help contextualize the observed heterogeneity in patient deviation profiles, particularly within the theta–beta functional space. Second, although we focused on resting-state MEG due to its availability and suitability for large-scale modeling, the normative modeling framework itself is equally applicable to task-based electrophysiological data. Task paradigms provide a powerful means to isolate specific cognitive functions, potentially increasing clinical interpretability by probing domain-specific neural processes[101,24,102]. Extending normative models to task data, an approach already gaining traction in fMRI[103], could enhance the specificity of functional deviation measures, contingent on the availability of sufficiently large and demographically diverse datasets. Finally, incorporating longitudinal data into normative models offers an additional layer of personalization by capturing individual trajectories over time. Methods such as velocity-based modeling[104] could improve sensitivity to subtle within-subject changes, enabling earlier detection of pathological deviations and more precise tracking of disease progression, critical for advancing precision medicine applications.

MEGaNorm provides a step toward individualized, transdiagnostic analysis of functional brain dynamics across the lifespan. By combining methodological rigor with clinical applicability, our framework lays the foundation for more precise, interpretable, and generalizable models of brain function. Although clinical application will require further development and rigorous validation, as normative modeling continues to evolve, we anticipate that MEGaNorm will serve as a valuable resource for both basic neuroscience and precision neuropsychiatry, helping to bridge the gap between supporting the translation of large-scale population data and person-centered clinical insight.

Methods

Datasets

Resting-state MEG (rs-MEG) data were aggregated from six publicly available datasets, comprising a total of 1,846 clinically undiagnosed participants from the general population (Table 2): the Cambridge

Centre for Aging and Neuroscience (Cam-CAN)[105], Boys Town National Research Hospital (BTH)[40], The Open MEG Archive (OMEGA)[106], the Human Connectome Project (HCP)[107], the National Institute of Mental Health (NIMH)[108], and the Mother Of Unification Studies (MOUS)[109]. Figure 5 shows the age distribution across these datasets. A total of 33 participants were excluded due to missing demographic information, absence of rs-MEG recordings, or convergence failures in the Spectral parameterization algorithm (see Supplementary Methods 1). All included participants were screened for neuropsychiatric conditions and evaluated as typically developing. In addition, we included rs-MEG recordings from 160 patients with Parkinson's disease available in the OMEGA dataset[106] (67 female; mean age = 59.93 years, SD = 15.59) to demonstrate the clinical applicability of the derived normative models. All patients had a diagnosis of mild to moderate idiopathic Parkinson's disease and were receiving a stable regimen of antiparkinsonian medication at the time of recording[88,110].

The data acquisition process varied across datasets in terms of MEG hardware configurations, sampling rates, and preprocessing procedures. For the Cam-CAN dataset, recordings were collected using a 306-channel Elekta MEGIN system comprising 102 magnetometers and 204 planar gradiometers, with a 1,000 Hz sampling rate. Real-time head position tracking was performed using four Head-Position Indicators (HPIs), and temporal Signal Space Separation (tSSS)[111] was applied using MaxFilter v2.2 (correlation threshold = 0.98, 10-second sliding window) to mitigate motion artifacts and external noise. Electrocardiogram (ECG) and electrooculogram (EOG) signals were also recorded to capture physiological activity. The BTH dataset was acquired using a similar Elekta MEGIN system (1,000 Hz sampling rate) with four HPIs, and tSSS was applied using MaxFilter v2.2 (correlation threshold = 0.95, 10-second sliding window). The OMEGA dataset utilized a 275-channel CTF axial-gradiometer system (CTF MEG, Coquitlam, BC, Canada) with a 2,400 Hz sampling rate, along with ECG and EOG recordings, and applied third-order gradient noise correction during acquisition to reduce environmental interference. The MOUS dataset was also acquired using a CTF system, with a 1,200 Hz sampling rate and accompanying ECG and EOG channels. Similarly, the NIMH dataset employed a CTF system with a 1,200 Hz sampling rate and third-order gradient noise correction. Finally, the HCP dataset was recorded using a Magnes 3600 system (4DNeuroimaging, San Diego, CA) with 248 magnetometers.

MEG preprocessing

MEG recordings were preprocessed using a pipeline designed to reduce noise and prepare the data for spectral analysis while accommodating variability in acquisition protocols across sites. Preprocessing began with the removal of bad channels to ensure signal quality before further analysis. First, channels previously marked as flat or noisy in the original datasets were excluded. For the Cam-CAN and BTH datasets, which were recorded using Elekta MEGIN systems, we used the MaxFilter-processed data after application of tSSS. In these datasets, noisy channels had already been identified and either reconstructed or excluded during acquisition. For the remaining datasets, recorded using CTF or Magnes systems, bad channel detection was performed using Maxwell filtering as implemented in MNE-Python[112]. Channels identified as excessively noisy or flat were removed before subsequent steps.

All recordings were resampled to 1,000 Hz if necessary and filtered using a finite impulse response

(FIR) filter with a 1 Hz high-pass and 45 Hz low-pass cutoff. A notch filter was applied to attenuate line noise. To reduce physiological artifacts, independent component analysis (ICA) was performed using the FastICA algorithm [113], as implemented in MNE-Python [112]. We used a data-driven approach based on variance-explained analysis with knee-point detection [114] as a heuristic to decide the number of components in ICA decomposition (see Supplementary Methods 2). To ensure physiologically relevant and artifactual signals were adequately captured, we retained 30 components (95.7% variance explained), balancing signal preservation with computational efficiency. When ECG recordings were available, Pearson correlation coefficients were calculated between each independent component and the ECG signal to identify components related to cardiac activity. In the absence of ECG data, a synthetic ECG reference was generated by averaging across magnetometers (for Elekta and Magnes systems) or gradiometers (for CTF systems). Components with correlation coefficients exceeding 0.9 were rejected. A similar procedure was used to identify and remove eye movement artifacts when EOG recordings were available. To minimize contamination from non-neural transients such as eye blinks or movements typically occurring at the start and end of sessions, the first and last 20 seconds of each recording were discarded. The remaining data were segmented into 10-second epochs with a 2-second overlap, creating standardized time windows for downstream spectral analysis.

Estimating power spectrum densities and IDP extraction

We first computed power spectral densities (PSDs) for each 10-second segment using Welch's method [115], employing a 2-second Hamming window with 1-second overlap and no zero-padding. The resulting PSDs were then averaged across all segments to yield a single PSD estimate per sensor, thereby enhancing the signal-to-noise ratio.

MEG recordings reflect both oscillatory (periodic) brain activity and broadband aperiodic signals. Consequently, raw PSDs can be confounded by background $1/f$ like structure (Figure 6a), where spectral power decays exponentially with frequency f [57]. To prevent the confounding effect of aperiodic activity, we first isolated periodic activity by subtracting the aperiodic activity (Figure 6b). This ensures that the extracted IDPs reflect true oscillatory brain activity. We then computed the relative periodic power for canonical frequency bands: theta (3–8 Hz), alpha (8–13 Hz), beta (13–30 Hz), and gamma (30–40 Hz) (Figure 6c). Relative power in each band was defined as the ratio of periodic power within that band to the total periodic power across the full 3–40 Hz range.

To isolate the periodic component, we used the Spectral parameterization (specparam, formerly fooof) algorithm (version 1.1.0) [44], which decomposes the PSD into periodic and aperiodic components (Figure 7b) by modeling the latter as an exponential function:

$$L = b - \log(k + F^{\chi}) \tag{1}$$

where b, F, and χ represent the broadband offset, frequency vector, and exponent, respectively. The parameter k captures the bend (or "knee") in the aperiodic component.

Incorporating the knee parameter ($k > 0$) into the fitting process significantly enhances the quality

of specparam model fits compared to the fixed mode ($k = 0$). Figure 7a shows that enabling the knee mode substantially increases the proportion of explained variance (R^2). When the model is fit in fixed mode, the aperiodic component can exceed the original power spectrum in certain frequency ranges, resulting in biologically implausible negative periodic power values (Figure 7b). Moreover, the average power spectrum across subjects and channels, plotted in log-log space, reveals a clear knee in the mid-frequency range (Figure 7c). The fixed mode, which imposes a single $1/f$ characteristic, appears as a straight line in log-log space and fails to capture this knee. In contrast, enabling the knee mode parameter allows models to more accurately represent this spectral bend, improving the quality of the fit.

To ensure the goodness of fits, the coefficient of determination R^2 is used as a quality control approach. This metric quantifies how much of the shape of the spectrum is captured by specparam's model. We excluded channels with $R^2 < 0.90$ from further analysis to ensure reliable aperiodic correction.

To obtain the IDPs, we spatially averaged them across all MEG sensors. This summarization step yielded four global IDPs per participant, each representing the relative periodic power in one of the canonical frequency bands across the entire brain. For recordings from Elekta MEGIN systems, we computed the average across both magnetometer and planar gradiometer channels, as these sensor types showed strong agreement in their spectral profiles (Pearson correlation; see Supplementary Figure 2). This sensor-level aggregation was necessary for harmonizing across recording devices and enabling consistent downstream modeling of spectral features. We use the MEGaNorm package (v0.1.0) [78] for MEG data processing and IDP extraction.

Normative modeling

Normative modeling is a statistical framework for characterizing the centiles of brain phenotypes across a population, analogous to pediatric growth charts [1,116]. The central idea is to detect abnormalities by first establishing the range of typical variation in a healthy reference population. This is accomplished by modeling the relationship between demographic or behavioral covariates (e.g., age) and the probability distributions of biological measurements. This is performed by estimating a mapping function f between covariates $\mathbf{X} \in \mathbb{R}^{n \times p}$, i.e., p covariates across n participants, and a response biological variable $\mathbf{y} \in \mathbb{R}^n$ (e.g., relative alpha power)):

$$\mathbf{y} = f(\mathbf{X}, \theta) + \epsilon \tag{2}$$

where θ and $\epsilon \sim \mathcal{G}(0, \sigma^2)$ denote model parameters and residuals, respectively. The estimated normative model can then be used to compute deviation scores that quantify how much an individual's measurement departs from the expected normative trajectory with respect to covariates in the form of z-scores $\mathbf{z} \in \mathbb{R}^n$:

$$\mathbf{z} = \frac{\mathbf{y} - f(\mathbf{X}, \theta)}{\sqrt{\sigma^2 + \sigma_*^2}} \tag{3}$$

where σ_*^2 represents the variations in the predictions due to parameter uncertainty. Larger absolute

values of z-scores indicate greater deviation from the expected normative range.

We used hierarchical Bayesian regression (HBR), implemented in the Predictive Clinical Neuroscience Toolkit (PCNtoolkit, version 0.35)[116], to estimate the mapping function f for the extracted IDPs. HBR was selected for its ability to account for site-related batch effects and its compatibility with federated learning architectures[5], enabling decentralized model updates without sharing individual-level data. Age was included as a continuous covariate, and to model non-linear age trajectories of IDPs, we applied a cubic B-spline basis expansion with five evenly spaced knots. Previous research has highlighted site-specific[117] and sex-specific[39] effects on age-related changes in IDPs. Therefore, we modeled sex and site as random intercepts to account for systematic differences in baseline power levels across subgroups. Including age, sex, and site as covariates helps minimize their influence on deviation estimates by regressing out their associated effects[5]. Eye condition (eyes open vs. closed) was not modeled as an explicit covariate because each dataset employed a single, consistent eye condition. As a result, eye condition is implicitly accounted for through the site-specific intercepts in the HBR model. Our results show that datasets recorded under eyes-open conditions (e.g., MOUS, OMEGA, NIMH) exhibit lower relative alpha power (see Supplementary Figure 3), consistent with prior findings[118,119]. This modeling strategy helps prevent potential confounding between eye condition and estimated variability in the population (see Supplementary Results 1 for statistical verification). To further accommodate heteroscedasticity, the variance was modeled as a function of age, allowing for age-dependent variability in the distribution of IDPs.

To accommodate non-Gaussian distributions in the data, we used a Sinh-Arcsinh (SHASH) likelihood[45], which generalizes the Gaussian distribution by introducing additional parameters for skewness and kurtosis. The SHASH distribution[50] is parameterized by four quantities: the mean (μ), scale (σ), skewness (ϵ), and kurtosis (δ), allowing flexible modeling of both the location and shape of the distribution (see Supplementary Methods 3). In our implementation, all four parameters were modeled as linear functions of age, enabling conditional estimation of both central tendency and distributional form. Posterior inference was performed using the No-U-Turn Sampler (NUTS)[120], as implemented in PyMC[121] version 5.22. In all analyses, we adopted the default settings for model hyperparameters (e.g., number of knots in B-spline and model priors) in the PCNToolkit package to avoid overfitting through manual hyperparameter selection.

Model evaluation

To assess the goodness of fit and calibration of the estimated normative centiles, we evaluated the trained models on a held-out test set using a range of diagnostic metrics. The dataset was split into 50% training and 50% testing subsets stratified by sites. This procedure was repeated 10 times using different random seeds to assess the robustness and generalizability of the models.

We evaluated both the accuracy of the fit and the quality of centile calibration, following established principles in normative modeling[122]. For model fit, we used the Standardized Mean Squared Error (SMSE) to quantify prediction accuracy. To assess the distributional correctness of the estimated centiles, we examined the Gaussianity of the derived z-scores using three complementary metrics: skewness, excess

kurtosis, and the Shapiro–Wilk test statistic (W)[51]. These metrics provide an indirect measure of centile quality by testing whether the z-scores conform to a standard normal distribution.

To directly evaluate centile calibration, we introduced a new metric, Mean Absolute Centile Error (MACE), which quantifies the average deviation between predicted and empirical centiles in the test set. Inspired by reliability diagrams, MACE measures the alignment of model-predicted quantiles with observed data quantiles (see Figure 8). The MACE metric is computed as follows:

$$\text{MACE} = \frac{1}{b}\sum_{k=1}^{b}\left(\frac{1}{m}\sum_{j=1}^{m}\left|q_j - \frac{\sum_{i=1}^{n}\mathbf{1}\{\hat{q}_{ij} \geq y_i\}}{n}\right|\right) \tag{4}$$

where b represents the number of batch effects (i.e., unique combinations of sex and site), and m denotes the number of centiles used for calibration. The terms q_j and $\hat{q}_{ij}$ represent the centile value and its corresponding predicted y-value for the ith data point, respectively. The term $\mathbf{1}\{\hat{q}_{ij} \geq y_i\}$ is an indicator function that outputs 0 or 1, depending on whether y_i lies below or above its predicted jth centile value. Summing these outputs across all data points and dividing them by the total number of data points, n, gives the actual centile corresponding to the jth predicted centile. By subtracting this from the true j-th centile, we can have an estimation of the deviation between the predicted and true centiles. In our experiments, we evaluate the MACE for the 1^{st}, 5^{th}, 25^{th}, 50^{th}, 75^{th}, 95^{th}, and 99^{th} centiles.

Anomaly detection

We assessed the clinical relevance of the derived normative models using an anomaly detection framework, in which large deviations from normative trajectories are interpreted as potential markers of pathology. Deviation scores (z) were computed for all patients and healthy participants in the test set of the OMEGA dataset. Following the approach proposed by Kia et al.[5], each z-score was converted into a probability of abnormality, $P_{\text{abn}}(z)$, by calculating the area under the standard Gaussian cumulative density function in the interval $[-|z|, |z|]$:

$$P_{\text{abn}}(z) = \frac{2}{\sqrt{2\pi}}\int_{|z|}^{\infty} e^{-t^2/2}\,dt - 1 \tag{5}$$

This transformation yields a continuous measure of abnormality for each IDP. To quantify discriminative performance, we computed the area under the receiver operating characteristic curve (AUC) for each feature, benchmarking abnormality probabilities against true clinical labels across test samples.

Statistics and Reproducibility

All preprocessing, model training, statistical analysis, and figure generation were performed using the open MEGaNorm package (`v.0.1.1`). Custom scripts are made publicly accessible (see Code Availability), enabling full computational reproducibility. Relative oscillatory power in canonical frequency bands was modeled using HBR, accounting for age, sex, and site. Site effects were modeled explicitly to accom-

modate multi-site variability, following established normative modeling approaches. Model performance was evaluated using held-out data and standard predictive accuracy metrics. To ensure robustness and reproducibility of results involving stochastic components (e.g., model initialization and optimization), all main analyses were repeated 10 times using different random seeds.

All datasets analyzed are publicly accessible through established repositories (see Data Availability), ensuring full transparency and independent reproducibility of the study. The primary dataset comprised 1,846 individuals aged 6–88 years aggregated from publicly available repositories. All participants represented independent observations; no repeated measures were included. For downstream clinical demonstration, the Parkinson's disease cohort consisted of 160 independent participants. Sample sizes were determined by data availability in the respective open repositories and were not predetermined by power calculations.

Data Availability

No new data were collected for this study. All datasets used in this study are publicly available from established open-access neuroimaging repositories. The Human Connectome Project (HCP Young Adult) dataset[107] is available from the Human Connectome Project repository at https://www.humanconnectome.org/study/hcp-young-adult. Access requires registration and agreement to the HCP data use terms. The Open MEG Archive (OMEGA) dataset[106] is available via the OMEGA repository, DOI: https://doi.org/10.23686/0015896. The National Institute of Mental Health (NIMH) dataset[108] is available from OpenNeuro under accession number `ds004215.v1.0.3` https://openneuro.org/datasets/ds005752/versions/2.1.0. The Cambridge Centre for Ageing and Neuroscience (Cam-CAN) dataset[105] is available through the Cam-CAN data portal at https://camcan-archive.mrc-cbu.cam.ac.uk/dataaccess/. Access requires an application and approval by the Cam-CAN data access committee. The Boys Town National Research Hospital (BTH) dataset[40] is publicly available via the data link provided in the original publication: https://cdn.boystown.org/media/Rempe_Ott_PNAS_2023_Data.zip. The Mother Of Unification Studies (MOUS) dataset[109] is available from the Radboud Data Repository, DOI: https://doi.org/10.34973/37n0-yc51. We gratefully acknowledge the considerable open-science efforts of the neuroimaging community in making these datasets publicly available. This work would not have been possible without the commitment of these research teams to data sharing and transparent science.

All derived data underlying the figures and statistical analyses generated in this study will be made publicly available at https://github.com/ML4PNP/MEG_Norm. All other data supporting the findings of this study are available from the corresponding author upon reasonable request.

Code Availability

All custom code developed for data processing, model training, and analysis is openly available in the MEGaNorm GitHub repository and archived on Zenodo[78]. The code is released under the GNU General

Public License v3.0 and includes documentation for installation and usage. Scripts to reproduce the main analyses and figures in this paper are provided in the paper GitHub repository at https://github.com/ML4PNP/MEG_Norm. Additionally, we plan to openly share the derived normative models via the PCNPortal for model extension and adaptation to new datasets.

Competing interests

The authors declare no competing interests.

Acknowledgments

S.M.K. gratefully acknowledges the starter grant for the "MEGaNorm" project, funded by the Dutch Ministry of Education, Culture and Science under the National Sector Plan. S.M.K. further acknowledges NWA Innovative projects within the routes grant (NWA.1418.24.006) and Small Compute Applications grant (EINF-8659) from the Netherlands Organization for Scientific Research (NWO). S.M.K. thanks the Digital Sciences for Society program at Tilburg University for the Growth Project grant (DSFS 202417) supporting the project "Charting the Normative Electroencephalography in Healthy Aging Population".

Author Contributions

MZ and SMK conceived the study, developed the methodology, implemented the software, performed the formal analyses, curated the data, conducted the investigation, and generated the visualizations. YV, AdB, and AM contributed to methodology development and software design. AM, TR, TW, RD, MŠP, and MvW contributed to conceptual development and investigation. SMK, MvW, and MŠP were involved in the supervision. SMK acquired funding and provided resources. MZ drafted the original manuscript. All authors reviewed and edited the manuscript and approved the final version.

References

[1] Andre F Marquand, Iead Rezek, Jan Buitelaar, and Christian F Beckmann. Understanding heterogeneity in clinical cohorts using normative models: beyond case-control studies. *Biological psychiatry*, 80(7):552–561, 2016.

[2] Andre F Marquand, Seyed Mostafa Kia, Mariam Zabihi, Thomas Wolfers, Jan K Buitelaar, and Christian F Beckmann. Conceptualizing mental disorders as deviations from normative functioning. *Molecular psychiatry*, 24(10):1415–1424, 2019.

[3] Ashlea Segal, Jeggan Tiego, Linden Parkes, Avram J Holmes, Andre F Marquand, and Alex Fornito. Embracing variability in the search for biological mechanisms of psychiatric illness. *Trends in Cognitive Sciences*, 29(1):85–99, 2025.

[4] Andre F Marquand, Thomas Wolfers, Maarten Mennes, Jan Buitelaar, and Christian F Beckmann. Beyond lumping and splitting: a review of computational approaches for stratifying psychiatric disordersbeyond lumping and splitting. *Neuroinformatics*, 2016.

[5] Seyed Mostafa Kia, Hester Huijsdens, Saige Rutherford, Augustijn de Boer, Richard Dinga, Thomas Wolfers, Pierre Berthet, Maarten Mennes, Ole A Andreassen, Lars T Westlye, et al. Closing the life-cycle of normative modeling using federated hierarchical bayesian regression. *Plos one*, 17(12):e0278776, 2022.

[6] Saige Rutherford, Charlotte Fraza, Richard Dinga, Seyed Mostafa Kia, Thomas Wolfers, Mariam Zabihi, Pierre Berthet, Amanda Worker, Serena Verdi, Derek Andrews, et al. Charting brain growth and aging at high spatial precision. *elife*, 11:e72904, 2022.

[7] Ramona Cirstian, Natalie Forde, Gary Zhang, Gerhard S Hellemann, Christian F Beckmann, Nina V Kraguljac, and Andre F Marquand. Lifespan normative models of white matter fractional anisotropy: Applications to early psychosis. *bioRxiv*, pages 2024–12, 2024.

[8] Julio E Villalon Reina, Alyssa H Zhu, Sebastian Benavidez, Clara E Moreau, Yixue Feng, Tamoghna Chattopadhyay, Leila Nabulsi, Leila Kushan, John P John, Himanshu Joshi, et al. Lifespan normative modeling of brain microstructure. *bioRxiv*, pages 2024–12, 2024.

[9] Thomas Wolfers, Nhat Trung Doan, Tobias Kaufmann, Dag Alnæs, Torgeir Moberget, Ingrid Agartz, Jan K Buitelaar, Torill Ueland, Ingrid Melle, Barbara Franke, et al. Mapping the heterogeneous phenotype of schizophrenia and bipolar disorder using normative models. *JAMA psychiatry*, 75(11):1146–1155, 2018.

[10] Pierre Berthet, Beathe C Haatveit, Rikka Kjelkenes, Amanda Worker, Seyed Mostafa Kia, Thomas Wolfers, Saige Rutherford, Dag Alnaes, Richard Dinga, Mads L Pedersen, et al. A 10-year longitudinal study of brain cortical thickness in people with first-episode psychosis using normative models. *Schizophrenia Bulletin*, 51(1):95–107, 2025.

[11] Mariam Zabihi, Marianne Oldehinkel, Thomas Wolfers, Vincent Frouin, David Goyard, Eva Loth, Tony Charman, Julian Tillmann, Tobias Banaschewski, Guillaume Dumas, et al. Dissecting the heterogeneous cortical anatomy of autism spectrum disorder using normative models. *Biological psychiatry: cognitive neuroscience and neuroimaging*, 4(6):567–578, 2019.

[12] Serena Verdi, Seyed Mostafa Kia, Keir XX Yong, Duygu Tosun, Jonathan M Schott, Andre F Marquand, and James H Cole. Revealing individual neuroanatomical heterogeneity in Alzheimer's disease using neuroanatomical normative modeling. *Neurology*, 100(24):e2442–e2453, 2023.

[13] Flavia Loreto, Serena Verdi, Seyed Mostafa Kia, Aleksandar Duvnjak, Haneen Hakeem, Anna Fitzgerald, Neva Patel, Johan Lilja, Zarni Win, Richard Perry, et al. Alzheimer's disease heterogeneity revealed by neuroanatomical normative modeling. *Alzheimer's & Dementia: Diagnosis, Assessment & Disease Monitoring*, 16(1):e12559, 2024.

[14] Thomas Insel, Bruce Cuthbert, Marjorie Garvey, Robert Heinssen, Daniel S Pine, Kevin Quinn, Charles Sanislow, and Philip Wang. Research domain criteria (rdoc): toward a new classification framework for research on mental disorders, 2010.

[15] Eva Češková and Petr Šilhán. From personalized medicine to precision psychiatry? *Neuropsychiatric Disease and Treatment*, pages 3663–3668, 2021.

[16] Peter J Uhlhaas, Peter Liddle, David EJ Linden, Anna C Nobre, Krish D Singh, and Joachim Gross. Magnetoencephalography as a tool in psychiatric research: current status and perspective. *Biological Psychiatry: Cognitive Neuroscience and Neuroimaging*, 2(3):235–244, 2017.

[17] Matthew M Nour, Yunzhe Liu, and Raymond J Dolan. Functional neuroimaging in psychiatry and the case for failing better. *Neuron*, 110(16):2524–2544, 2022.

[18] Bradford C Dickerson. Advances in functional magnetic resonance imaging: technology and clinical applications. *Neurotherapeutics*, 4(3):360–370, 2007.

[19] Timothy Lawn, Alessio Giacomel, Daniel Martins, Mattia Veronese, Matthew Howard, Federico E Turkheimer, and Ottavia Dipasquale. Normative modelling of molecular-based functional circuits captures clinical heterogeneity transdiagnostically in psychiatric patients. *Communications Biology*, 7(1):689, 2024.

[20] Ashlea Segal, Linden Parkes, Kevin Aquino, Seyed Mostafa Kia, Thomas Wolfers, Barbara Franke, Martine Hoogman, Christian F Beckmann, Lars T Westlye, Ole A Andreassen, et al. Regional, circuit and network heterogeneity of brain abnormalities in psychiatric disorders. *Nature Neuroscience*, 26(9):1613–1629, 2023.

[21] Janus RL Kobbersmed, Chetan Gohil, Andre Marquand, and Diego Vidaurre. One-shot normative modelling of whole-brain functional connectivity. *bioRxiv*, pages 2025–01, 2025.

[22] Sylvain Baillet. Magnetoencephalography for brain electrophysiology and imaging. *Nature neuroscience*, 20(3):327–339, 2017.

[23] Michael X Cohen. Where does EEG come from and what does it mean? *Trends in neurosciences*, 40(4):208–218, 2017.

[24] Ryouhei Ishii, Leonides Canuet, Yasunori Aoki, Masahiro Hata, Masao Iwase, Shunichiro Ikeda, Keiichiro Nishida, and Manabu Ikeda. Healthy and pathological brain aging: from the perspective of oscillations, functional connectivity, and signal complexity. *Neuropsychobiology*, 75(4):151–161, 2018.

[25] Yoji Hirano and Peter J Uhlhaas. Current findings and perspectives on aberrant neural oscillations in schizophrenia. *Psychiatry and clinical neurosciences*, 75(12):358–368, 2021.

[26] Christian Beste, Alexander Münchau, and Christian Frings. Towards a systematization of brain oscillatory activity in actions. *Communications Biology*, 6(1):137, 2023.

[27] Erwin Roy John, LS Prichep, J Fridman, and P Easton. Neurometrics: computer-assisted differential diagnosis of brain dysfunctions. *Science*, 239(4836):162–169, 1988.

[28] Thomas Koenig, Leslie Prichep, Dietrich Lehmann, Pedro Valdes Sosa, Elisabeth Braeker, Horst Kleinlogel, Robert Isenhart, and E Roy John. Millisecond by millisecond, year by year: normative EEG microstates and developmental stages. *Neuroimage*, 16(1):41–48, 2002.

[29] Marco Congedo, Roy E John, Dirk De Ridder, and Leslie Prichep. Group independent component analysis of resting state EEG in large normative samples. *International Journal of Psychophysiology*, 78(2):89–99, 2010.

[30] Carol L Wilkinson, Lisa D Yankowitz, Jerry Y Chao, Rodrigo Gutiérrez, Jeff L Rhoades, Shlomo Shinnar, Patrick L Purdon, and Charles A Nelson. Developmental trajectories of EEG aperiodic and periodic components in children 2–44 months of age. *Nature communications*, 15(1):5788, 2024.

[31] Marius Tröndle, Tzvetan Popov, Andreas Pedroni, Christian Pfeiffer, Zofia Barańczuk-Turska, and Nicolas Langer. Decomposing age effects in EEG alpha power. *Cortex*, 161:116–144, 2023.

[32] J Ko, U Park, D Kim, and SW Kang. Quantitative electroencephalogram standardization: A sex-and age-differentiated normative database. front. neurosci. 15, 766781, 2021.

[33] Dinavahi VPS Murty, Keerthana Manikandan, Wupadrasta Santosh Kumar, Ranjini Garani Ramesh, Simran Purokayastha, Mahendra Javali, Naren Prahalada Rao, and Supratim Ray. Gamma oscillations weaken with age in healthy elderly in human EEG. *NeuroImage*, 215:116826, 2020.

[34] Carlos Gómez, Jose M Perez-Macias, Jesús Poza, Alberto Fernández, and Roberto Hornero. Spectral changes in spontaneous MEG activity across the lifespan. *Journal of neural engineering*, 10 (6):066006, 2013.

[35] BAE Hunt, SM Wong, MM Vandewouw, MJ Brookes, BT Dunkley, and MJ Taylor. Spatial and spectral trajectories in typical neurodevelopment from childhood to middle age. netw. neurosci. 3, 497–520, 2019.

[36] Justyna Gula, Victoria Moiseeva, Maria Herrojo Ruiz, and Marinella Cappelletti. Characterizing the middle-age neurophysiology using EEG/MEG. *bioRxiv*, pages 2021–06, 2021.

[37] Bikash Sahoo, Anagh Pathak, Gustavo Deco, Arpan Banerjee, and Dipanjan Roy. Lifespan associated global patterns of coherent neural communication. *Neuroimage*, 216:116824, 2020.

[38] Kusum Thuwal, Arpan Banerjee, and Dipanjan Roy. Aperiodic and periodic components of ongoing oscillatory brain dynamics link distinct functional aspects of cognition across adult lifespan. *Eneuro*, 8(5), 2021.

[39] Lauren R Ott, Samantha H Penhale, Brittany K Taylor, Brandon J Lew, Yu-Ping Wang, Vince D Calhoun, Julia M Stephen, and Tony W Wilson. Spontaneous cortical MEG activity undergoes unique age-and sex-related changes during the transition to adolescence. *NeuroImage*, 244:118552, 2021.

[40] Maggie P Rempe, Lauren R Ott, Giorgia Picci, Samantha H Penhale, Nicholas J Christopher-Hayes, Brandon J Lew, Nathan M Petro, Christine M Embury, Mikki Schantell, Hallie J Johnson, et al. Spontaneous cortical dynamics from the first years to the golden years. *Proceedings of the National Academy of Sciences*, 120(4):e2212776120, 2023.

[41] Veera Itälinna, Hanna Kaltiainen, Nina Forss, Mia Liljeström, and Lauri Parkkonen. Using normative modeling and machine learning for detecting mild traumatic brain injury from magnetoencephalography data. *PLoS computational biology*, 19(11):e1011613, 2023.

[42] T Hinault, S Baillet, and SM Courtney. Age-related changes of deep-brain neurophysiological activity. *Cerebral Cortex*, 33(7):3960–3968, 2023.

[43] Marius Tröndle, Tzvetan Popov, Sabine Dziemian, and Nicolas Langer. Decomposing the role of alpha oscillations during brain maturation. *ELife*, 11:e77571, 2022.

[44] Thomas Donoghue, Matar Haller, Erik J Peterson, Paroma Varma, Priyadarshini Sebastian, Richard Gao, Torben Noto, Antonio H Lara, Joni D Wallis, Robert T Knight, et al. Parameterizing neural power spectra into periodic and aperiodic components. *Nature neuroscience*, 23 (12):1655–1665, 2020.

[45] Augustijn AA de Boer, Johanna MM Bayer, Seyed Mostafa Kia, Saige Rutherford, Mariam Zabihi, Charlotte Fraza, Pieter Barkema, Lars T Westlye, Ole A Andreassen, Max Hinne, et al. Non-gaussian normative modelling with hierarchical bayesian regression. *Imaging Neuroscience*, 2:1–36, 2024.

[46] Shirin Heidari, Thomas F Babor, Paola De Castro, Sera Tort, and Mirjam Curno. Sex and gender equity in research: rationale for the sager guidelines and recommended use. *Research integrity and peer review*, 1:1–9, 2016.

[47] Karla L Miller, Fidel Alfaro-Almagro, Neal K Bangerter, David L Thomas, Essa Yacoub, Junqian Xu, Andreas J Bartsch, Saad Jbabdi, Stamatios N Sotiropoulos, Jesper LR Andersson, et al. Multimodal population brain imaging in the uk biobank prospective epidemiological study. *Nature neuroscience*, 19(11):1523–1536, 2016.

[48] Lloyd T Elliott, Kevin Sharp, Fidel Alfaro-Almagro, Sinan Shi, Karla L Miller, Gwenaëlle Douaud, Jonathan Marchini, and Stephen M Smith. Genome-wide association studies of brain imaging phenotypes in uk biobank. *Nature*, 562(7726):210–216, 2018.

[49] Johanna MM Bayer, Richard Dinga, Seyed Mostafa Kia, Akhil R Kottaram, Thomas Wolfers, Jinglei Lv, Andrew Zalesky, Lianne Schmaal, and Andre Marquand. Accommodating site variation

in neuroimaging data using normative and hierarchical bayesian models. *NeuroImage*, 264:119699, 2022.

[50] M Chris Jones and Arthur Pewsey. Sinh-arcsinh distributions. *Biometrika*, 96(4):761–780, 2009.

[51] Samuel Sanford Shapiro and Martin B Wilk. An analysis of variance test for normality (complete samples). *Biometrika*, 52(3-4):591–611, 1965.

[52] Yoav Benjamini and Yosef Hochberg. Controlling the false discovery rate: a practical and powerful approach to multiple testing. *Journal of the Royal Statistical Society: Series B (Methodological)*, 57(1):289–300, 1995.

[53] Donald B Lindsley. A longitudinal study of the occipital alpha rhythm in normal children: frequency and amplitude standards. *The Pedagogical Seminary and Journal of Genetic Psychology*, 55(1):197–213, 1939.

[54] Hideyuki Hoshi and Yoshihito Shigihara. Age-and gender-specific characteristics of the resting-state brain activity: a magnetoencephalography study. *Aging (Albany, NY)*, 12(21):21613, 2020.

[55] Eleni L Vlahou, Franka Thurm, Iris-Tatjana Kolassa, and Winfried Schlee. Resting-state slow wave power, healthy aging and cognitive performance. *Scientific reports*, 4(1):5101, 2014.

[56] Mikhail Ustinin, Anna Boyko, and Stanislav Rykunov. Healthy aging changes in conventional frequency bands of neuroelectric brain activity reconstructed from resting-state MEG. *GeroScience*, pages 1–16, 2025.

[57] Moritz Gerster, Gunnar Waterstraat, Vladimir Litvak, Klaus Lehnertz, Alfons Schnitzler, Esther Florin, Gabriel Curio, and Vadim Nikulin. Separating neural oscillations from aperiodic 1/f activity: challenges and recommendations. *Neuroinformatics*, 20(4):991–1012, 2022.

[58] Wei He, Thomas Donoghue, Paul F Sowman, Robert A Seymour, Jon Brock, Stephen Crain, Bradley Voytek, and Arjan Hillebrand. Co-increasing neuronal noise and beta power in the developing brain. *BioRxiv*, page 839258, 2019.

[59] Aron T Hill, Gillian M Clark, Felicity J Bigelow, Jarrad AG Lum, and Peter G Enticott. Periodic and aperiodic neural activity displays age-dependent changes across early-to-middle childhood. *Developmental Cognitive Neuroscience*, 54:101076, 2022.

[60] Fabian Schmidt, Sarah K Danböck, Eugen Trinka, Dominic P Klein, Gianpaolo Demarchi, and Nathan Weisz. Age-related changes in "cortical" 1/f dynamics are linked to cardiac activity. *bioRxiv*, pages 2022–11, 2022.

[61] Janna D Lendner, Randolph F Helfrich, Bryce A Mander, Luis Romundstad, Jack J Lin, Matthew P Walker, Pal G Larsson, and Robert T Knight. An electrophysiological marker of arousal level in humans. *elife*, 9:e55092, 2020.

[62] Sonia Montemurro, Daniel Borek, Daniele Marinazzo, Sara Zago, Fabio Masina, Ettore Napoli, Nicola Filippini, and Giorgio Arcara. Aperiodic component of EEG power spectrum and cognitive performance are modulated by education in aging. *Scientific Reports*, 14(1):15111, 2024.

[63] Anna J Finley, Douglas J Angus, Erik L Knight, Carien M van Reekum, Margie E Lachman, Richard J Davidson, and Stacey M Schaefer. Resting EEG periodic and aperiodic components predict cognitive decline over 10 years. *Journal of Neuroscience*, 44(13), 2024.

[64] Ashley Merkin, Sabrina Sghirripa, Lynton Graetz, Ashleigh E Smith, Brenton Hordacre, Richard Harris, Julia Pitcher, John Semmler, Nigel C Rogasch, and Mitchell Goldsworthy. Do age-related differences in aperiodic neural activity explain differences in resting EEG alpha? *Neurobiology of Aging*, 121:78–87, 2023.

[65] Anna J Finley, Douglas J Angus, Carien M van Reekum, Richard J Davidson, and Stacey M Schaefer. Periodic and aperiodic contributions to theta-beta ratios across adulthood. *Psychophysiology*, 59(11):e14113, 2022.

[66] Thomas Donoghue. A systematic review of aperiodic neural activity in clinical investigations. *medRxiv*, pages 2024–10, 2024.

[67] Jelena Bozek, Ludovica Griffanti, Stephan Lau, and Mark Jenkinson. Normative models for neuroimaging markers: Impact of model selection, sample size and evaluation criteria. *Neuroimage*, 268:119864, 2023.

[68] Christos Davatzikos. Machine learning in neuroimaging: Progress and challenges. *Neuroimage*, 197:652–656, 2019.

[69] Felicha T Candelaria-Cook, Isabel Solis, Megan E Schendel, Yu-Ping Wang, Tony W Wilson, Vince D Calhoun, and Julia M Stephen. Developmental trajectory of MEG resting-state oscillatory activity in children and adolescents: a longitudinal reliability study. *Cerebral Cortex*, 32(23):5404–5419, 2022.

[70] Maggie P Rempe, Brandon J Lew, Christine M Embury, Nicholas J Christopher-Hayes, Mikki Schantell, and Tony W Wilson. Spontaneous sensorimotor beta power and cortical thickness uniquely predict motor function in healthy aging. *NeuroImage*, 263:119651, 2022.

[71] Andrey P Anokhin, Viktor Müller, Ulman Lindenberger, Andrew C Heath, and Erin Myers. Genetic influences on dynamic complexity of brain oscillations. *Neuroscience letters*, 397(1-2):93–98, 2006.

[72] Lucy Foulkes and Sarah-Jayne Blakemore. Studying individual differences in human adolescent brain development. *Nature neuroscience*, 21(3):315–323, 2018.

[73] Richard Gao, Ruud L Van den Brink, Thomas Pfeffer, and Bradley Voytek. Neuronal timescales are functionally dynamic and shaped by cortical microarchitecture. *elife*, 9:e61277, 2020.

[74] Theo Gasser, Petra Bächer, and Joachim Möcks. Transformations towards the normal distribution of broad band spectral parameters of the EEG. *Electroencephalography and clinical neurophysiology*, 53(1):119–124, 1982.

[75] Theo Gasser, Rolf Verleger, Petra Bächer, and Lothar Sroka. Development of the EEG of school-age children and adolescents. i. analysis of band power. *Electroencephalography and clinical neurophysiology*, 69(2):91–99, 1988.

[76] Junting Ren, Susan Tapert, Chun Chieh Fan, and Wesley K Thompson. A semi-parametric bayesian model for semi-continuous longitudinal data. *Statistics in medicine*, 41(13):2354–2374, 2022.

[77] C Gaiser, P Berthet, SM Kia, MA Frens, CF Beckmann, RL Muetzel, and Andre F Marquand. Estimating cortical thickness trajectories in children across different scanners using transfer learning from normative models. *Human Brain Mapping*, 45(2):e26565, 2024.

[78] Mohammad Zamanzadeh, Ymke Verduyn, and Seyed Mostafa Kia. MEGaNorm: a Python package for normative modeling on MEG and EEG data, May 2025. URL https://doi.org/10.5281/zenodo.15441320.

[79] Pieter Barkema, Saige Rutherford, Hurng-Chun Lee, Seyed Mostafa Kia, Hannah Savage, Christian Beckmann, and Andre Marquand. Predictive clinical neuroscience portal (pcnportal): instant online access to research-grade normative models for clinical neuroscientists. *Wellcome open research*, 8:326, 2023.

[80] Lennard I Boon, Victor J Geraedts, Arjan Hillebrand, Martijn R Tannemaat, Maria Fiorella Contarino, Cornelis J Stam, and Henk W Berendse. A systematic review of MEG-based studies in Parkinson's disease: The motor system and beyond. *Human brain mapping*, 40(9):2827–2848, 2019.

[81] Ned Jenkinson and Peter Brown. New insights into the relationship between dopamine, beta oscillations and motor function. *Trends in neurosciences*, 34(12):611–618, 2011.

[82] Arun Singh and Stella M Papa. Aberrant striatal oscillations after dopamine loss in parkinsonian non-human primates. *bioRxiv*, page 650770, 2019.

[83] Srdjan Sumarac, Jinyoung Youn, Conor Fearon, Luka Zivkovic, Prerana Keerthi, Oliver Flouty, Milos Popovic, Mojgan Hodaie, Suneil Kalia, Andres Lozano, et al. Clinico-physiological correlates of parkinson's disease from multi-resolution basal ganglia recordings. *npj Parkinson's Disease*, 10 (1):175, 2024.

[84] D Stoffers, JLW Bosboom, JB Deijen, E Ch Wolters, HW Berendse, and CJ Stam. Slowing of oscillatory brain activity is a stable characteristic of parkinson's disease without dementia. *Brain*, 130(7):1847–1860, 2007.

[85] JLW Bosboom, D Stoffers, CJ Stam, BW Van Dijk, J Verbunt, HW Berendse, and E Ch Wolters. Resting state oscillatory brain dynamics in parkinson's disease: an MEG study. *Clinical Neurophysiology*, 117(11):2521–2531, 2006.

[86] B Pollok, V Krause, W Martsch, C Wach, A Schnitzler, and M Südmeyer. Motor-cortical oscillations in early stages of parkinson's disease. *The Journal of Physiology*, 590(13):3203–3212, 2012.

[87] Elizabeth Heinrichs-Graham, Max J Kurz, Katherine M Becker, Pamela M Santamaria, Howard E Gendelman, and Tony W Wilson. Hypersynchrony despite pathologically reduced beta oscillations in patients with parkinson's disease: a pharmaco-magnetoencephalography study. *Journal of Neurophysiology*, 112(7):1739–1747, 2014.

[88] Gillian Roberts, Samuel Hardy, Robert Chen, Benjamin T Dunkley, and PREVENT-AD Research Group & Quebec Parkinson Network. Individual cases of parkinson's disease can be robustly classified by cortical oscillatory activity from magnetoencephalography. *medRxiv*, pages 2024–08, 2024.

[89] Mikkel C Vinding, Josefine Waldthaler, Allison Eriksson, Cassia Low Manting, Daniel Ferreira, Martin Ingvar, Per Svenningsson, and Daniel Lundqvist. Oscillatory and non-oscillatory features of the magnetoencephalic sensorimotor rhythm in parkinson's disease. *npj Parkinson's Disease*, 10 (1):51, 2024.

[90] Mikkel C Vinding, Panagiota Tsitsi, Josefine Waldthaler, Robert Oostenveld, Martin Ingvar, Per Svenningsson, and Daniel Lundqvist. Reduction of spontaneous cortical beta bursts in parkinson's disease is linked to symptom severity. *Brain Communications*, 2(1):fcaa052, 2020.

[91] Pascal Helson, Daniel Lundqvist, Per Svenningsson, Mikkel C Vinding, and Arvind Kumar. Cortex-wide topography of 1/f-exponent in parkinson's disease. *npj Parkinson's Disease*, 9(1):109, 2023.

[92] Dana Pourzinal, Ji Hyun J Yang, Gerard J Byrne, John D O'Sullivan, Leander Mitchell, Katie L McMahon, David A Copland, and Nadeeka N Dissanayaka. Identifying subtypes of mild cognitive impairment in parkinson's disease using cluster analysis. *Journal of Neurology*, 267(11):3213–3222, 2020.

[93] Eric Feczko, Oscar Miranda-Dominguez, Mollie Marr, Alice M Graham, Joel T Nigg, and Damien A Fair. The heterogeneity problem: approaches to identify psychiatric subtypes. *Trends in cognitive sciences*, 23(7):584–601, 2019.

[94] Anita Pal, Nishi Pegwal, Madhuri Behari, and Ratna Sharma. High delta and gamma EEG power in resting state characterise dementia in parkinson's patients. *Biomarkers in Neuropsychiatry*, 3: 100027, 2020.

[95] Alberto Fernandez, Agustin Turrero, Pilar Zuluaga, Pedro Gil-Gregorio, Francisco del Pozo, Fernando Maestu, and Stephan Moratti. MEG delta mapping along the healthy aging-alzheimer's disease continuum: diagnostic implications. *Journal of Alzheimer's disease*, 35(3):495–507, 2013.

[96] Haiguang Wen and Zhongming Liu. Separating fractal and oscillatory components in the power spectrum of neurophysiological signal. *Brain topography*, 29:13–26, 2016.

[97] Marios Antonakakis, Sophie Schrader, Ümit Aydin, Asad Khan, Joachim Gross, Michalis Zervakis, Stefan Rampp, and Carsten H Wolters. Inter-subject variability of skull conductivity and thickness in calibrated realistic head models. *Neuroimage*, 223:117353, 2020.

[98] Hannah McCann, Giampaolo Pisano, and Leandro Beltrachini. Variation in reported human head tissue electrical conductivity values. *Brain topography*, 32(5):825–858, 2019.

[99] Chunyan Cao, Dianyou Li, Shikun Zhan, Chencheng Zhang, Bomin Sun, and Vladimir Litvak. L-dopa treatment increases oscillatory power in the motor cortex of parkinson's disease patients. *NeuroImage: Clinical*, 26:102255, 2020.

[100] Olivier B Simon, Donald C Rojas, Debashis Ghosh, Xinyi Yang, Sarah E Rogers, Christine S Martin, Samantha K Holden, Benzi M Kluger, and Isabelle Buard. Profiling parkinson's disease cognitive phenotypes via resting-state magnetoencephalography. *Journal of neurophysiology*, 127 (1):279–289, 2022.

[101] Bradley Voytek, Mark A Kramer, John Case, Kyle Q Lepage, Zechari R Tempesta, Robert T Knight, and Adam Gazzaley. Age-related changes in 1/f neural electrophysiological noise. *Journal of neuroscience*, 35(38):13257–13265, 2015.

[102] Dinavahi VPS Murty, Keerthana Manikandan, Wupadrasta Santosh Kumar, Ranjini Garani Ramesh, Simran Purokayastha, Bhargavi Nagendra, Abhishek Ml, Aditi Balakrishnan, Mahendra Javali, Naren Prahalada Rao, et al. Stimulus-induced gamma rhythms are weaker in human elderly with mild cognitive impairment and alzheimer's disease. *Elife*, 10:e61666, 2021.

[103] Hannah S Savage, Peter CR Mulders, Philip FP Van Eijndhoven, Jasper Van Oort, Indira Tendolkar, Janna N Vrijsen, Christian F Beckmann, and Andre F Marquand. Dissecting task-based fMRI activity using normative modelling: an application to the emotional face matching task. *Communications biology*, 7(1):888, 2024.

[104] Charlotte Fraza, Saige Rutherford, Barbora Rehák Bučková, Christian F Beckmann, and Andre F Marquand. The promise of quantifying individual risk for brain disorders through normative modeling, a narrative review. *Neuroscience & Biobehavioral Reviews*, page 106284, 2025.

[105] Jason R Taylor, Nitin Williams, Rhodri Cusack, Tibor Auer, Meredith A Shafto, Marie Dixon, Lorraine K Tyler, Richard N Henson, et al. The Cambridge Centre for Ageing and Neuroscience (Cam-CAN) data repository: Structural and functional MRI, MEG, and cognitive data from a cross-sectional adult lifespan sample. *neuroimage*, 144:262–269, 2017.

[106] Guiomar Niso, Christine Rogers, Jeremy T Moreau, Li-Yuan Chen, Cecile Madjar, Samir Das, Elizabeth Bock, François Tadel, Alan C Evans, Pierre Jolicoeur, et al. OMEGA: the open MEG archive. *Neuroimage*, 124:1182–1187, 2016.

[107] David C Van Essen, Kamil Ugurbil, Edward Auerbach, Deanna Barch, Timothy EJ Behrens, Richard Bucholz, Acer Chang, Liyong Chen, Maurizio Corbetta, Sandra W Curtiss, et al. The human connectome project: a data acquisition perspective. *Neuroimage*, 62(4):2222–2231, 2012.

[108] Allison C Nugent, Adam G Thomas, Margaret Mahoney, Alison Gibbons, Jarrod T Smith, Antoinette J Charles, Jacob S Shaw, Jeffrey D Stout, Anna M Namyst, Arshitha Basavaraj, et al. The NIMH intramural healthy volunteer dataset: A comprehensive MEG, MRI, and behavioral resource. *Scientific Data*, 9(1):518, 2022.

[109] Jan-Mathijs Schoffelen, Robert Oostenveld, Nietzsche HL Lam, Julia Uddén, Annika Hultén, and Peter Hagoort. A 204-subject multimodal neuroimaging dataset to study language processing. *Scientific data*, 6(1):17, 2019.

[110] Alex I Wiesman, Jason da Silva Castanheira, Clotilde Degroot, Edward A Fon, Sylvain Baillet, Quebec Parkinson Network, Prevent-Ad Research Group, et al. Adverse and compensatory neurophysiological slowing in parkinson's disease. *Progress in neurobiology*, 231:102538, 2023.

[111] Samu Taulu, Juha Simola, and Matti Kajola. Applications of the signal space separation method. *IEEE Transactions on Signal Processing*, 53(9):3359–3372, 2005.

[112] Alexandre Gramfort, Martin Luessi, Eric Larson, Denis A Engemann, Daniel Strohmeier, Christian Brodbeck, Roman Goj, Mainak Jas, Teon Brooks, Lauri Parkkonen, et al. MEG and EEG data analysis with MNE-Python. *Frontiers in Neuroinformatics*, 7:267, 2013.

[113] Aapo Hyvarinen. Fast and robust fixed-point algorithms for independent component analysis. *IEEE Transactions on Neural Networks*, 10(3):626–634, 1999.

[114] Ville Satopaa, Jeannie Albrecht, David Irwin, and Barath Raghavan. Finding a" kneedle" in a haystack: Detecting knee points in system behavior. In *2011 31st international conference on distributed computing systems workshops*, pages 166–171. IEEE, 2011.

[115] Peter Welch. The use of fast fourier transform for the estimation of power spectra: a method based on time averaging over short, modified periodograms. *IEEE Transactions on Audio and Electroacoustics*, 15(2):70–73, 1967.

[116] Saige Rutherford, Seyed Mostafa Kia, Thomas Wolfers, Charlotte Fraza, Mariam Zabihi, Richard Dinga, Pierre Berthet, Amanda Worker, Serena Verdi, Henricus G Ruhe, et al. The normative modeling framework for computational psychiatry. *Nature protocols*, 17(7):1711–1734, 2022.

[117] Alberto Jaramillo-Jimenez, Diego A Tovar-Rios, Yorguin-Jose Mantilla-Ramos, John-Fredy Ochoa-Gomez, Laura Bonanni, and Kolbjørn Brønnick. Combat models for harmonization of resting-state EEG features in multisite studies. *Clinical Neurophysiology*, 167:241–253, 2024.

[118] Nathan M Petro, Lauren R Ott, Samantha H Penhale, Maggie P Rempe, Christine M Embury, Giorgia Picci, Yu-Ping Wang, Julia M Stephen, Vince D Calhoun, and Tony W Wilson. Eyes-closed versus eyes-open differences in spontaneous neural dynamics during development. *NeuroImage*, 258: 119337, 2022.

[119] DPX Kan, PE Croarkin, CK Phang, and PF Lee. EEG differences between eyes-closed and eyes-open conditions at the resting stage for euthymic participants. *Neurophysiology*, 49(6):432–440, 2017.

[120] Matthew D Hoffman and Andrew Gelman. The no-u-turn sampler: adaptively setting path lengths in hamiltonian monte carlo. *J. Mach. Learn. Res.*, 15(1):1593–1623, 2014.

[121] Oriol Abril-Pla, Virgile Andreani, Colin Carroll, Larry Dong, Christopher J Fonnesbeck, Maxim Kochurov, Ravin Kumar, Junpeng Lao, Christian C Luhmann, Osvaldo A Martin, et al. Pymc: a modern, and comprehensive probabilistic programming framework in python. *PeerJ Computer Science*, 9:e1516, 2023.

[122] Richard Dinga, Charlotte J Fraza, Johanna MM Bayer, Seyed Mostafa Kia, Christian F Beckmann, and Andre F Marquand. Normative modeling of neuroimaging data using generalized additive models of location scale and shape. *BioRxiv*, pages 2021–06, 2021.

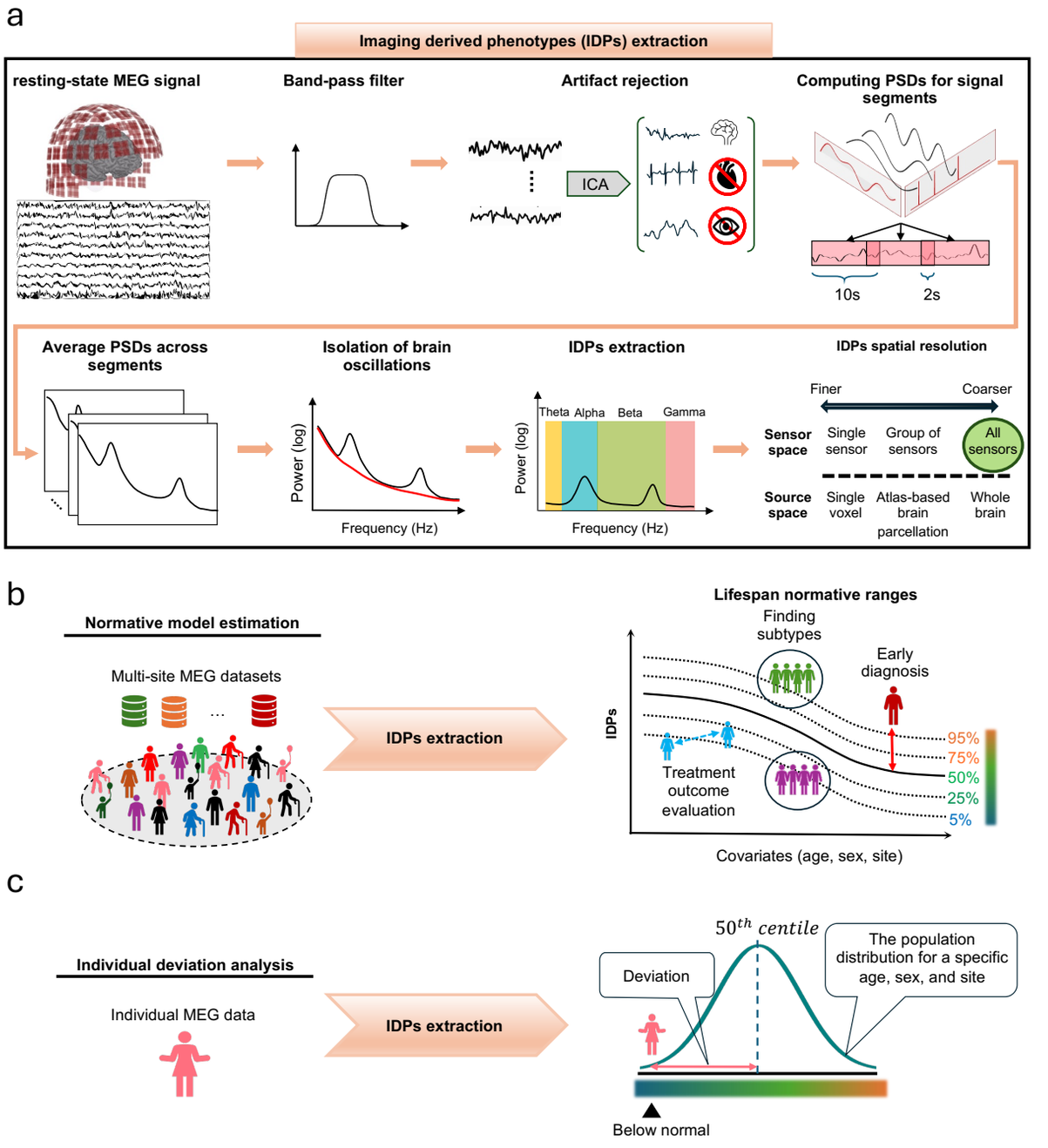

Figure 1: Overview of the MEGaNorm pipeline. MEGaNorm is an end-to-end framework for deriving normative models of resting-state MEG (rs-MEG) oscillations and quantifying individual deviations from population-level norms. The pipeline includes the extraction of functional imaging-derived phenotypes (IDPs), modeling normative trajectories across the lifespan, and characterizing individual-level deviations. **(a)** Signal preprocessing and IDP extraction: Raw rs-MEG signals undergo bandpass filtering and artifact removal using independent component analysis (ICA). Data are segmented into fixed-length epochs, and power spectral densities (PSDs) are computed and averaged across segments. Periodic activity is isolated by separating aperiodic components, and relative power is extracted in canonical frequency bands. These band-specific features are then averaged across sensors to obtain device-agnostic IDPs. **(b)** Normative model estimation: IDPs extracted from a large, multi-site cohort are used to estimate lifespan trajectories using hierarchical Bayesian regression. These models yield age-specific normative centiles for each frequency band, taking into account site and sex effects. The resulting normative ranges can support clinical applications such as early diagnosis, treatment monitoring, and subtyping of neuropsychiatric disorders. **(c)** Individual deviation analysis: For a new individual, IDPs are computed and compared against normative models conditioned on age, sex, and recording site. This enables the quantification and visualization of individualized deviations from normative trajectories. The article's Creative Commons license does not cover icons sourced from the Microsoft PowerPoint stock image library. All other elements are original.

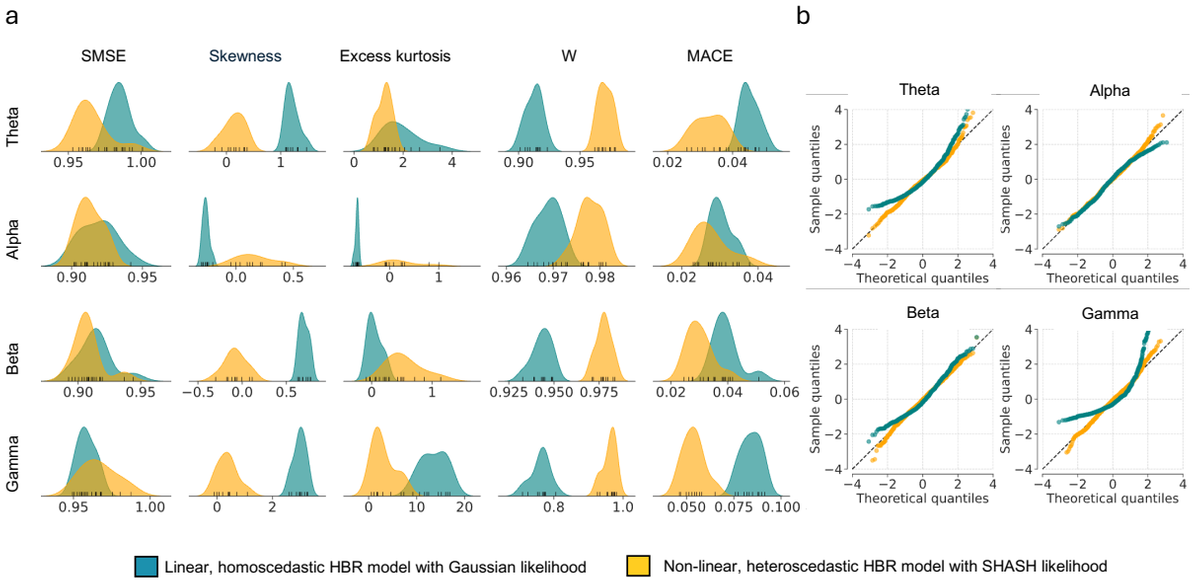

Figure 2: Model evaluation and comparison. **(a)** Summary of out-of-sample model diagnostics for four frequency-specific IDPs: standardized mean squared error (SMSE), skewness, excess kurtosis (kurtosis minus 3), Shapiro–Wilk test statistic W, and mean absolute centile error (MACE). Lower SMSE values reflect a more accurate estimation of the true central tendency with the baseline at 1. Skewness and excess kurtosis values closer to zero, along with W values closer to 1, reflect greater normality of the z-score distributions. Lower MACE values indicate better centile calibration. Here, the MACE was evaluated at the 1^{st}, 5^{th}, 25^{th}, 50^{th}, 75^{th}, 95^{th}, and 99^{th} centiles. Across all IDPs, the proposed non-linear, heteroscedastic, and non-Gaussian HBR model outperformed the baseline in modeling the distribution of response variables. **(b)** Q–Q plots of z-scores from the held-out test set. The black dashed 1:1 line represents the theoretical quantile–quantile correspondence under a standard Gaussian distribution. The proposed model shows closer adherence to Gaussianity compared to the baseline.

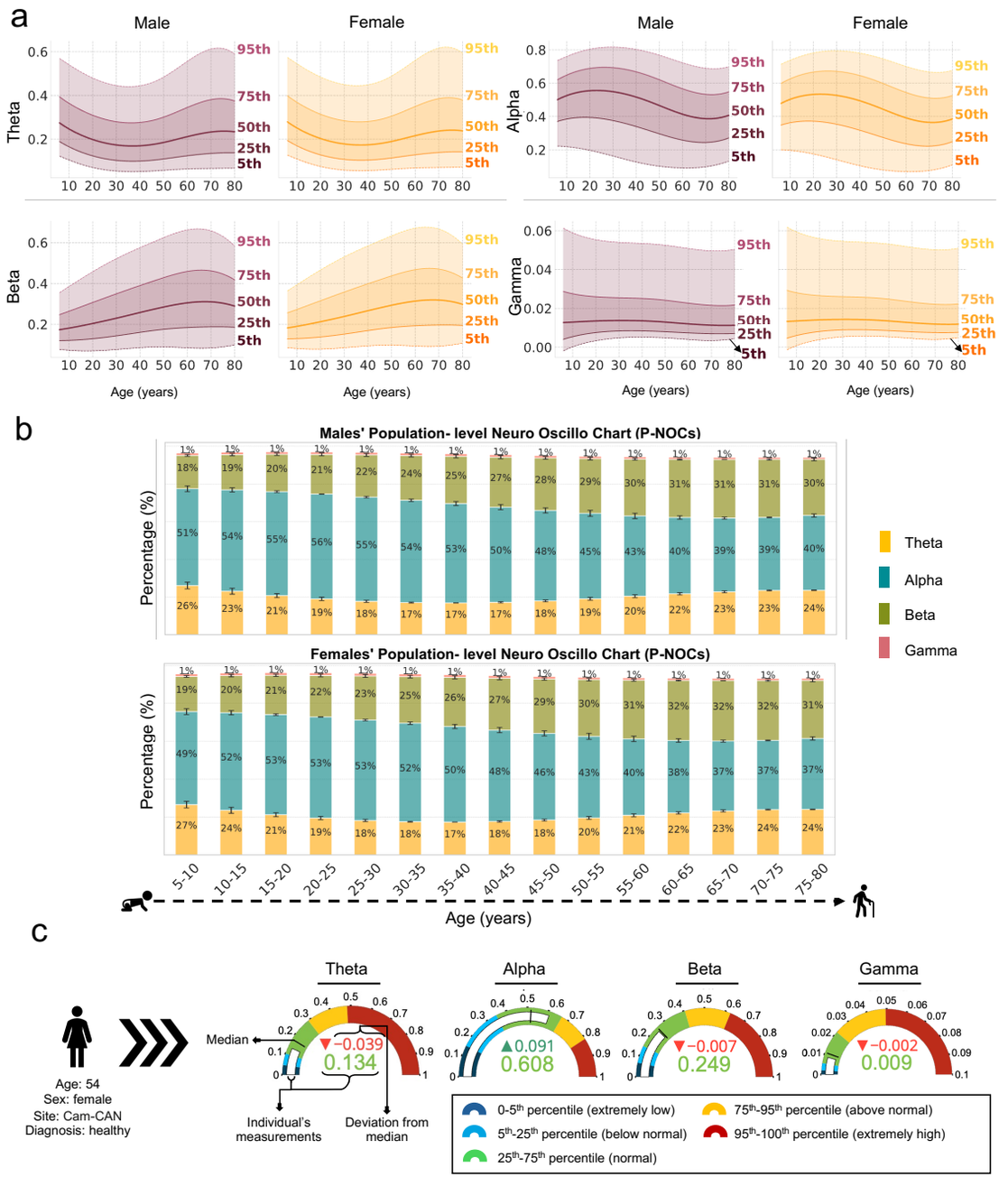

Figure 3: From growth charts to population- and individual-level Neuro-Oscillo Charts. (a) Lifespan growth charts for each frequency band (theta, alpha, beta, and gamma), stratified by sex. For visualization purposes, centiles were averaged across datasets. **(b)** Population-level Neuro-Oscillo Charts (P-NOCs), which depict the distribution of relative power across frequency bands at the 50^{th} centile, separately for males and females. To construct P-NOCs, median estimates are averaged within non-overlapping 5-year age bins. Due to non-linear changes within each age bin, reflected in the error bars indicating the standard deviation, the sum of the averaged values may deviate slightly from 100%. P-NOCs summarize how much the spectral power of each frequency band contributes to the total oscillatory power and how it evolves with aging, enabling intuitive comparisons of population-level trends across sex and lifespan. **(c)** Individual-level Neuro-Oscillo Charts (I-NOCs), which visualize a participant's spectral power relative to age-, sex-, and site-matched normative distributions derived from the growth charts. The white bar represents the participant's measurement, which is also shown by numerical values below the gauge plot (color-coded by the respective range). The upper value below the gauge plots displays the participant's measurement deviation from the 50^{th} percentile (shown by the black line). This example uses data from a clinically undiagnosed 54-year-old female participant from the Cam-CAN dataset. Centiles across frequency bands were derived by conditioning the normative ranges on the participant's age, sex, and site, representing the norm of 54-year-old females from Cam-CAN. The article's Creative Commons license does not cover icons sourced from the Microsoft PowerPoint stock image library. All other elements are original.

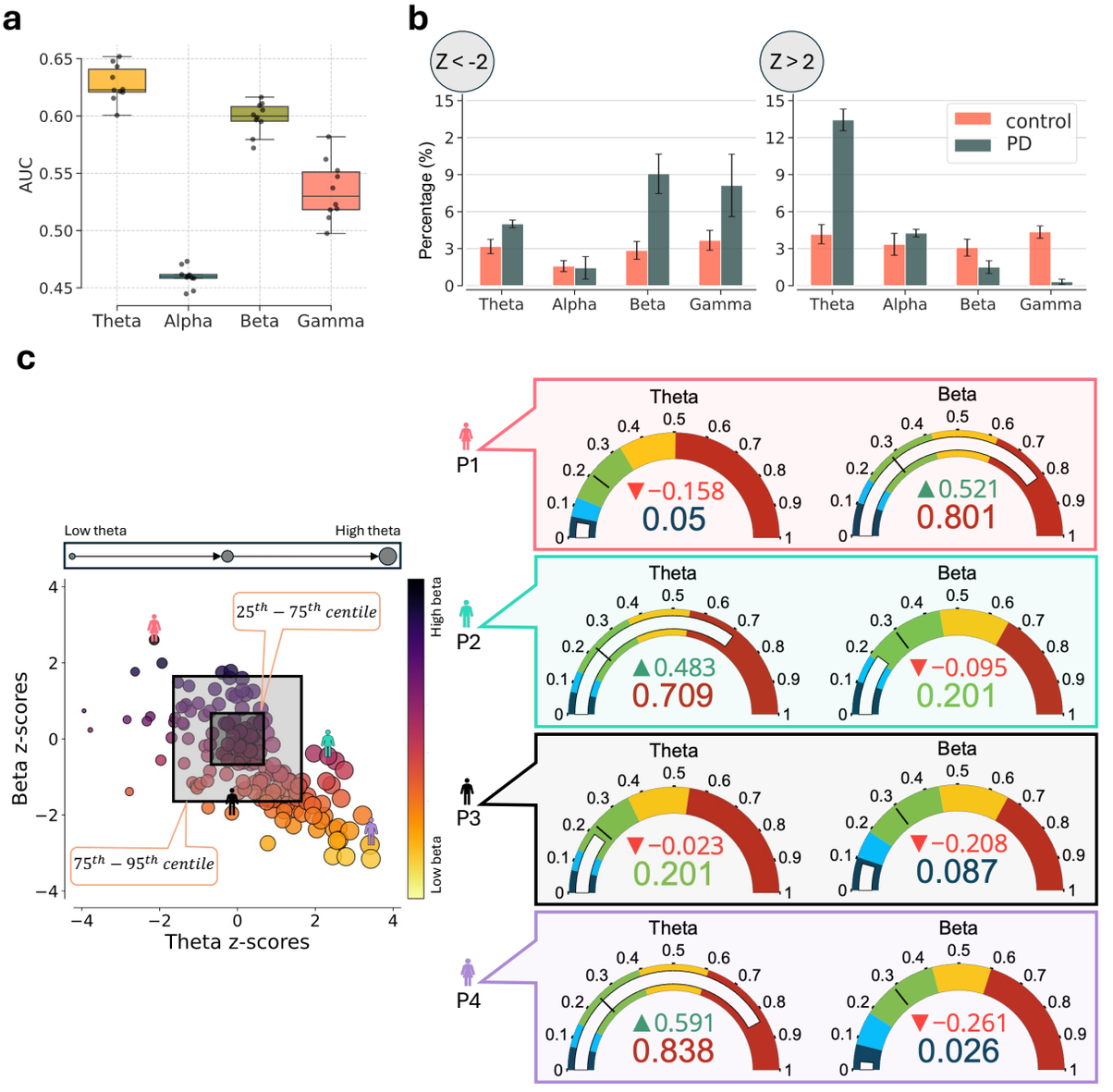

Figure 4: Individual-level analysis in the clinical population with Parkinson's disease. **(a)** Area under the ROC curves (AUCs) for anomaly detection across ten independent train–test splits. Z-score deviations were used to compute abnormal probability indices for each frequency band. **(b)** Percentage of participants exhibiting positive ($Z > 2$) and negative ($Z < -2$) extreme deviations across frequency bands, shown separately for healthy controls and patients. Bars represent averages over ten iterations; error bars indicate 95% confidence interval. **(c)** Scatter plot of patients in theta–beta deviation space. Marker size encodes theta z-scores (x-axis), and color encodes beta z-scores (y-axis). Selected individuals (P1–P4) illustrate distinct regions of this spectrum and are accompanied by their corresponding I-NOCs. The article's Creative Commons license does not cover icons sourced from the Microsoft PowerPoint stock image library. All other elements are original.

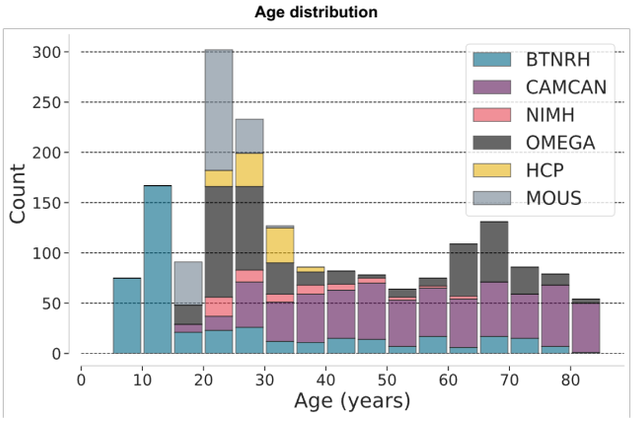

Figure 5: The age distribution of undiagnosed participants across the six datasets. The data spans a broad range of the human lifespan, from childhood (6 years) to late adulthood (88 years).

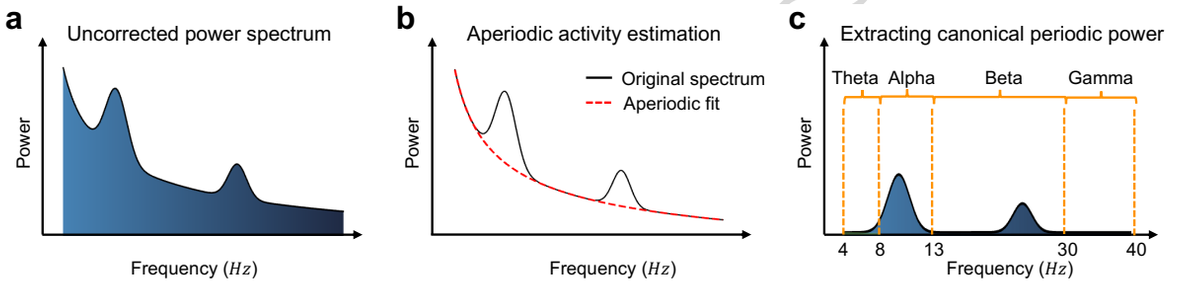

Figure 6: Extracting the relative power of the four canonical frequency bands. (a) The original power spectral density (PSD), encompassing both aperiodic and periodic activities. Spectral peaks reflect brain oscillations, while the broadband $1/f$ activity corresponds to the aperiodic component. **(b)** The aperiodic component (red dashed line) is estimated using an exponential function from the original PSD within the Spectral parameterization (specparam) algorithm. The aperiodic activity is then subtracted from the original PSD to isolate periodic activity. **(c)** Relative power of each canonical frequency band (theta, alpha, beta, gamma) is computed from the periodic activity as a proportion of the total periodic power between 3–40 Hz.

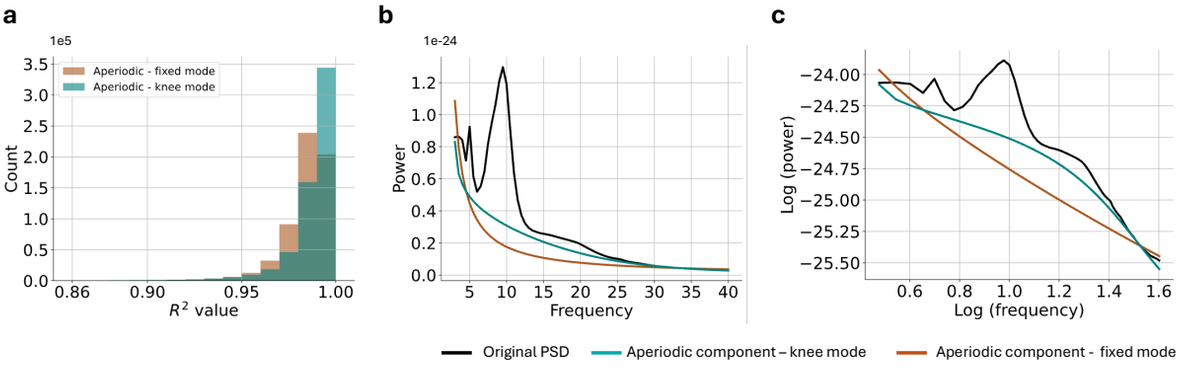

Figure 7: Parametrizing the bend ("knee") in aperiodic spectra improves specparam model fits. (a) Histogram of the coefficient of determination (R^2) for model fits across participants in both fixed mode ($k = 0$) and knee mode ($k > 0$). The knee mode yields a slightly higher R^2 value (median=0.99, SD=0.018) compared to the fixed mode (median=0.98, SD=0.019). **(b)** Average power spectrum across channels and participants (black line), alongside the corresponding estimated aperiodic components using both knee (teal line) and fixed (brown line) parameters, shown in linear space. At lower frequency ranges, the fixed-mode aperiodic fit overshoots the original PSD. **(c)** The same data shown in log-log space. The original PSD displays a clear bend in the middle frequency ranges. The fixed-mode fit (brown) fails to capture this bend, appearing as a straight line, while the knee-mode fit (teal) successfully models the curvature.

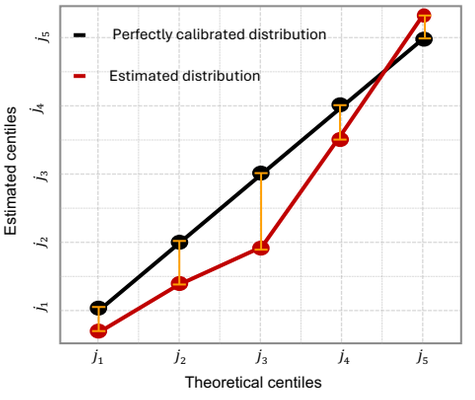

Figure 8: Schematic illustration of calculating the Mean Absolute Centile Error (MACE) to evaluate the quality of estimated centiles. The Reliability plot. The x-axis represents the i-th theoretical centile, while the y-axis shows the corresponding estimated centile. A well-calibrated model should align with the 1:1 diagonal line (shown in black). In this example, the estimated centiles (shown in red) deviate from the expected line. In MACE, we compute the difference between the theoretical and actual centiles for each j-th centile (orange lines) and then average these differences across all centiles.

Table 1: W statistics of Wilcoxon rank-sum test comparing the proposed (non-linear, heteroscedastic, and non-Gaussian) with the baseline HBR model (linear, homoscedastic, and Gaussian).

Metric	Theta	Alpha	Beta	Gamma
SMSE	-3.10^{**}	-0.98	-1.89	1.59
Skewness	-3.78^{***}	3.78^{***}	-3.78^{***}	-3.78^{***}
Kurtosis	-2.27^{*}	3.78^{***}	3.63^{***}	-3.78^{***}
Shapiro–Wilk test statistic	3.78^{***}	3.78^{***}	3.78^{***}	3.78^{***}
MACE	-3.78^{***}	-1.97^{*}	-3.25^{**}	-3.78^{***}

SMSE = standardized mean squared error; MACE = mean absolute centile error. Sample size, $n = 10$. Asterisks indicate statistical significance: * $p < 0.05$, ** $p < 0.01$, *** $p < 0.001$. All $p - values$ were corrected using false discovery rate (FDR) correction to account for multiple comparisons.

Table 2: Demographics and protocol of the datasets.

Scanner site	Participants	Female	Mean age	SD	Eyes	Duration	Country
MOUS [109]	199	101	22.02	2.94	EO	6 min	Netherlands
BTH [40]	433	204	25.16	20.52	EC	5–8 min	United States
Cam-CAN [105]	615	304	54.60	18.28	EC	8 min 40s	United Kingdom
NIMH [108]	66	45	34.16	11.96	EC	6 min	United States
OMEGA [106]	440	270	41.98	20.45	EO	5 min	Canada
HCP [107]	89	41	28.60	3.85	EO	6 min	United States

* Both the number of participants and females are reported after excluding individuals with missing information as described in Methods ; SD = standard deviation; EC = eyes closed; EO = eyes open.

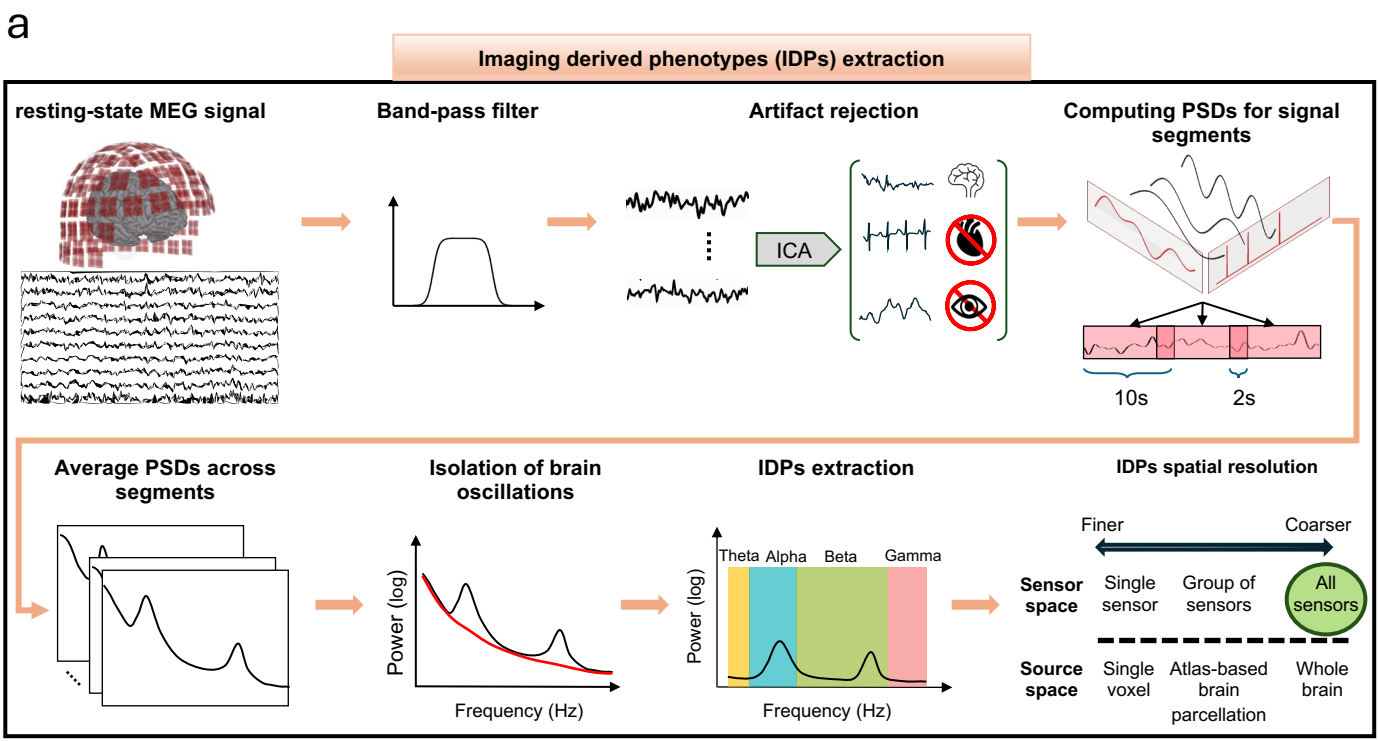
a
Imaging derived phenotypes (IDPs) extraction
resting-state MEG signal
Band-pass filter
Artifact rejection
ICA
Computing PSDs for signal segments
10s
2s
Average PSDs across segments
Isolation of brain oscillations
Power (log)
Frequency (Hz)
IDPs extraction
Theta Alpha Beta Gamma
Power (log)
Frequency (Hz)
IDPs spatial resolution
Finer
Coarser
Sensor space
Single sensor
Group of sensors
All sensors
Source space
Single voxel
Atlas-based brain parcellation
Whole brain

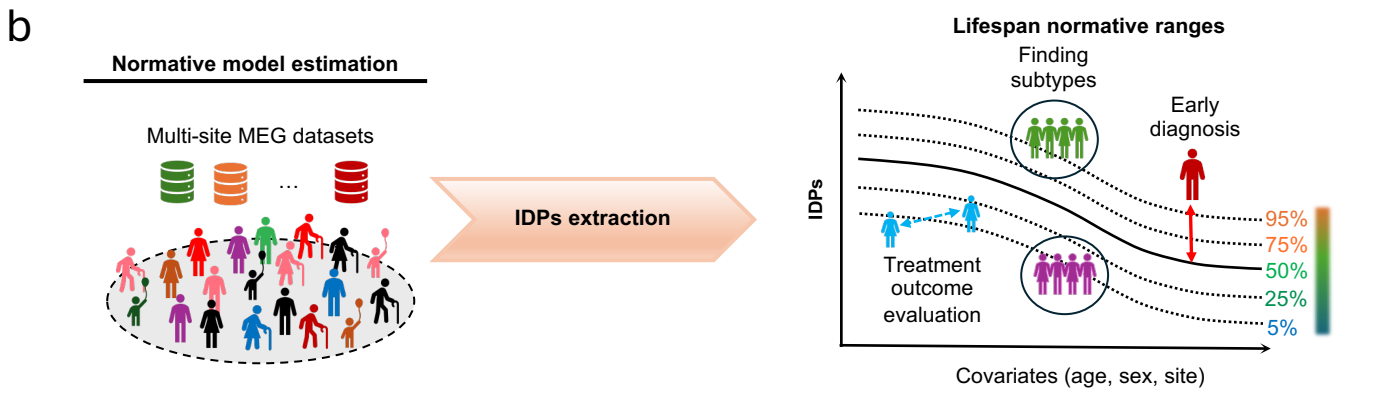
b
Normative model estimation
Multi-site MEG datasets
IDPs extraction
Lifespan normative ranges
Finding subtypes
Early diagnosis
IDPs
Treatment outcome evaluation
95%
75%
50%
25%
5%
Covariates (age, sex, site)

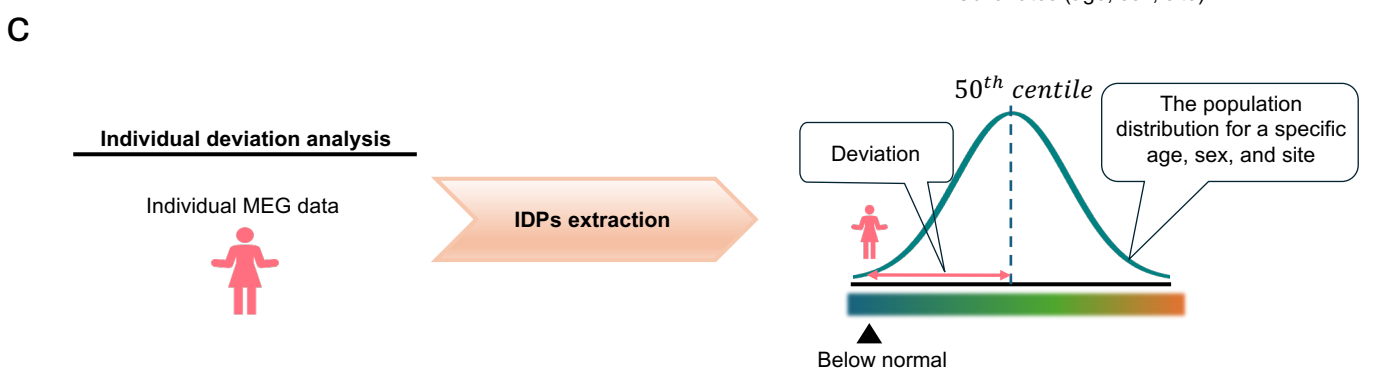
c
Individual deviation analysis
Individual MEG data
IDPs extraction
50th centile
The population distribution for a specific age, sex, and site
Deviation
Below normal

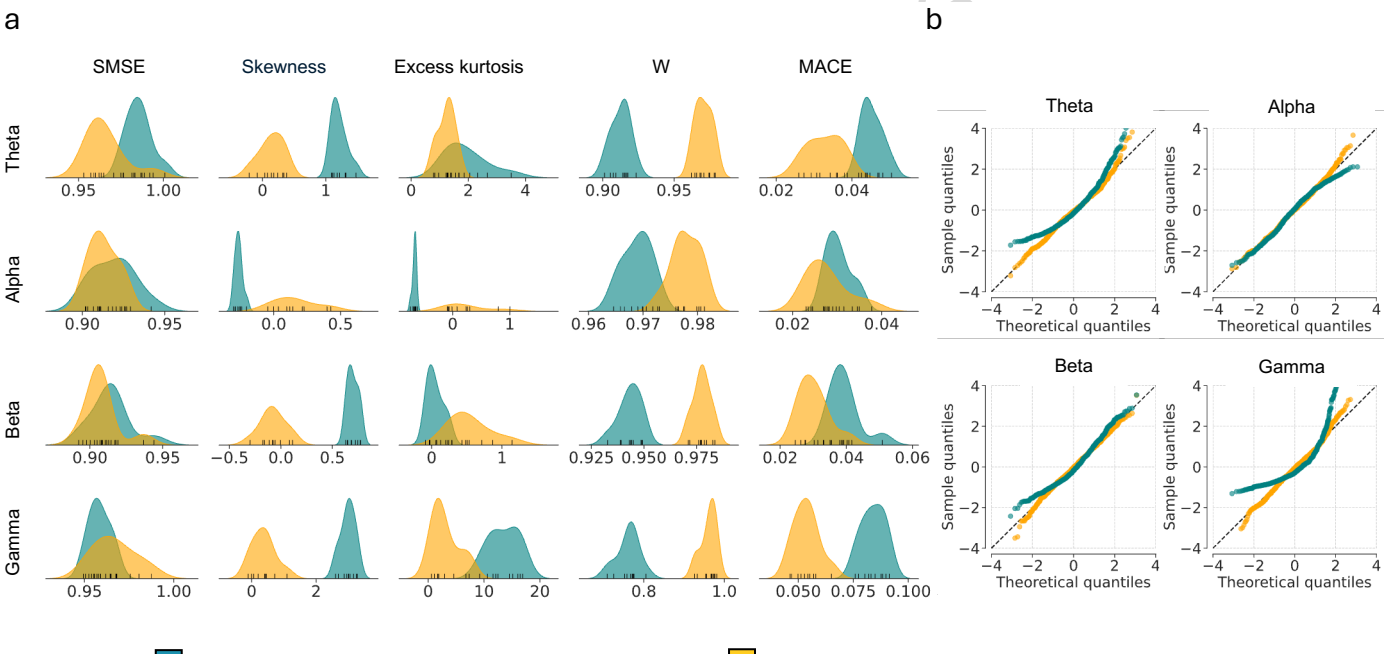

Linear, homoscedastic HBR model with Gaussian likelihood

Non-linear, heteroscedastic HBR model with SHASH likelihood

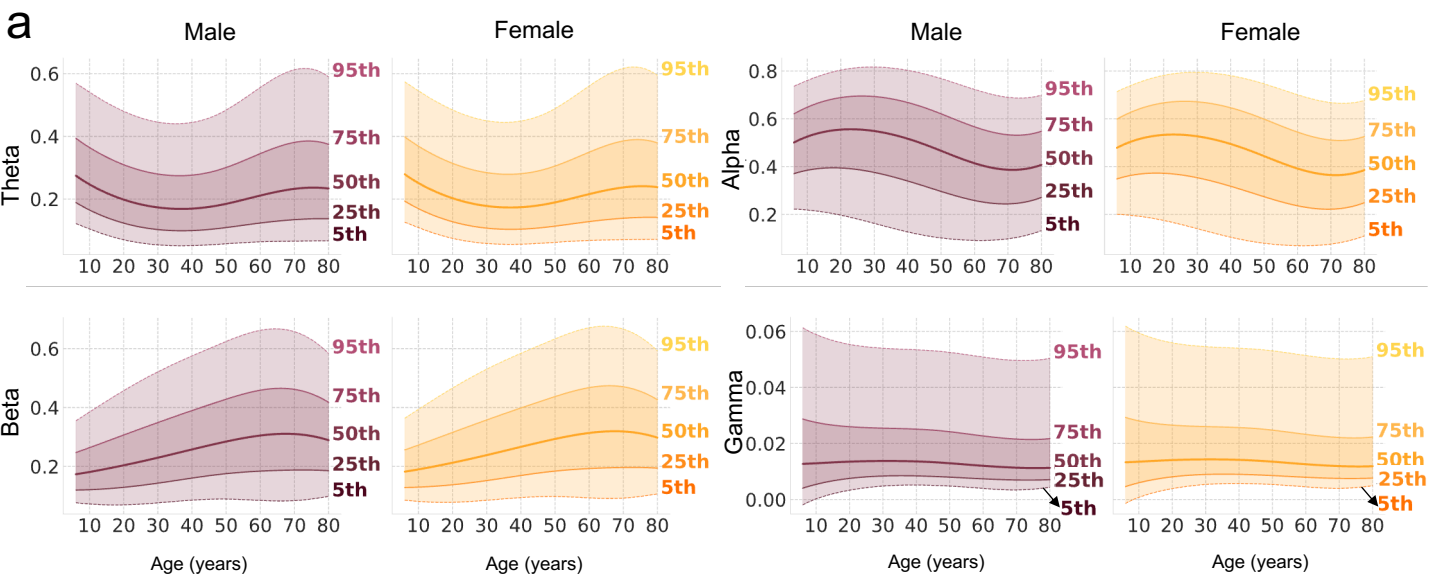
a
Male
Female
Male
Female
Theta
Alpha
Beta
Gamma
95th
75th
50th
25th
5th
Age (years)
Age (years)
Age (years)
Age (years)

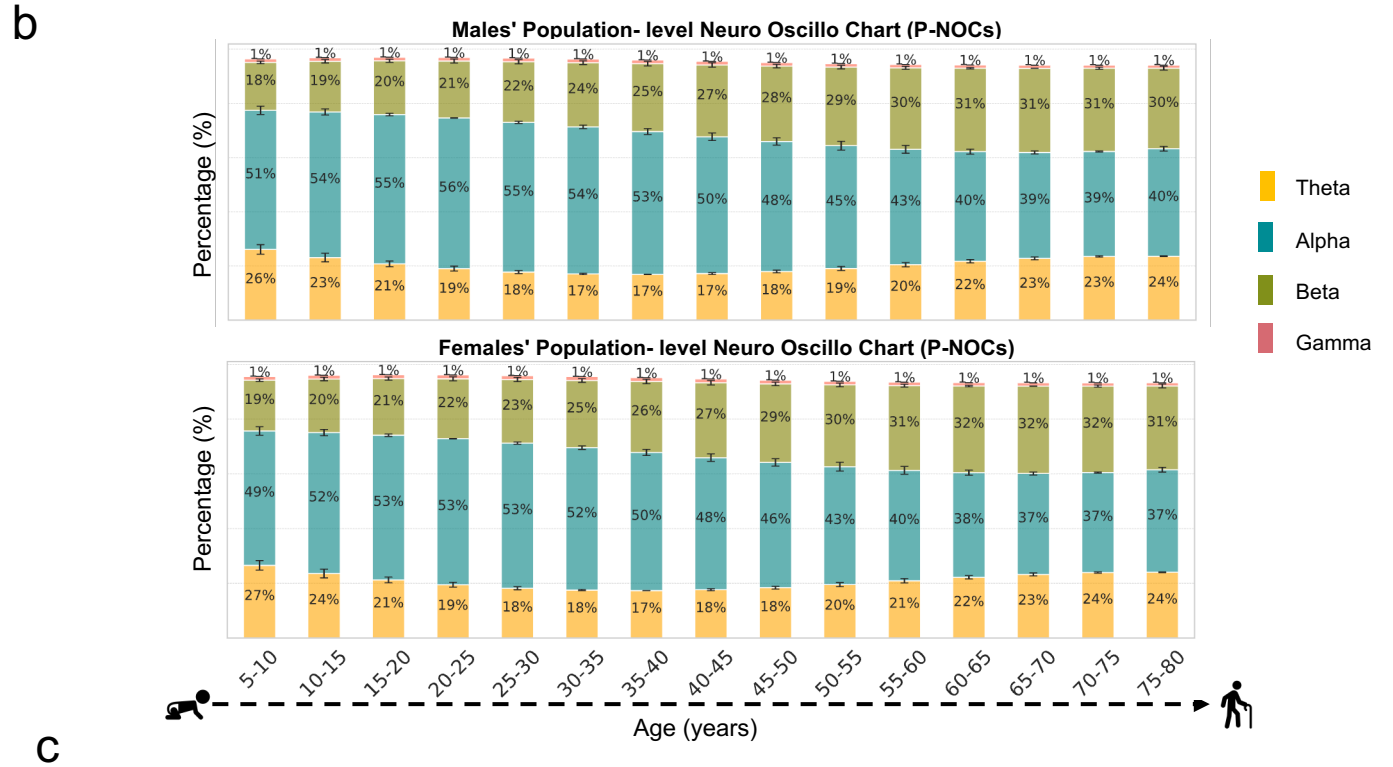
b
Males' Population- level Neuro Oscillo Chart (P-NOCs)
Females' Population- level Neuro Oscillo Chart (P-NOCs)
Percentage (%)
Percentage (%)
Theta
Alpha
Beta
Gamma
5-10
10-15
15-20
20-25
25-30
30-35
35-40
40-45
45-50
50-55
55-60
60-65
65-70
70-75
75-80
Age (years)

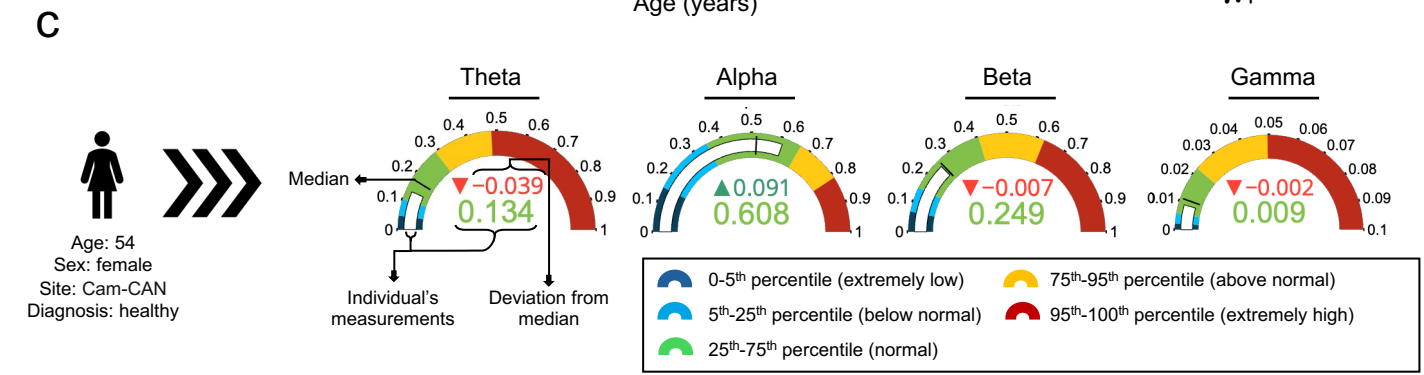
c
Age: 54
Sex: female
Site: Cam-CAN
Diagnosis: healthy
Theta
Alpha
Beta
Gamma
Median
▼−0.039
0.134
▲0.091
0.608
▼−0.007
0.249
▼−0.002
0.009
Individual's measurements
Deviation from median
0-5th percentile (extremely low)
5th-25th percentile (below normal)
25th-75th percentile (normal)
75th-95th percentile (above normal)
95th-100th percentile (extremely high)

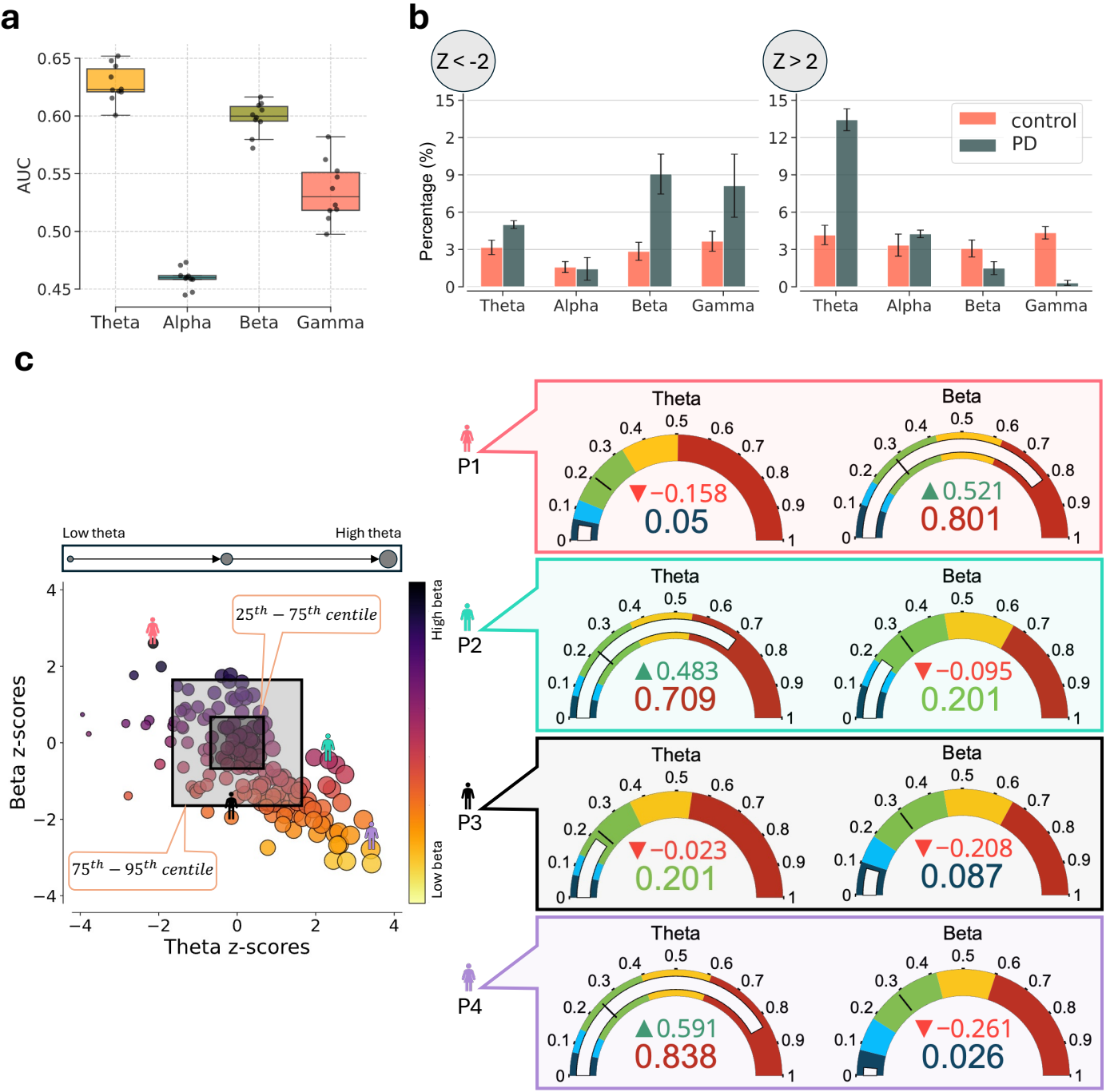
a
AUC
0.65
0.60
0.55
0.50
0.45
Theta
Alpha
Beta
Gamma
b
Z < -2
Z > 2
Percentage (%)
control
PD
Theta
Alpha
Beta
Gamma
c
Low theta
High theta
$25^{th} - 75^{th}$ centile
$75^{th} - 95^{th}$ centile
High beta
Low beta
Beta z-scores
Theta z-scores
P1
P2
P3
P4
Theta
Beta
−0.158
0.05
0.521
0.801
0.483
0.709
−0.095
0.201
−0.023
0.201
−0.208
0.087
0.591
0.838
−0.261
0.026